International Journal of Thermofluids 23 (2024) 100790

Contents lists available at ScienceDirect

International Journal of Thermofluids

journal homepage: www.sciencedirect.com/journal/international-journal-of-thermofluids

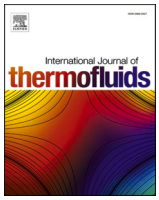

Effect of the building orientation on additively manufactured copper alloy: Hydraulic performance of different surface roughness channels

G. Favero [a,b,*], M. Bonesso [b], R. Dima [b], A. Pepato [b], F. Zanini [a], S. Carmignato [a], S. Mancin [a,b,c]

[a] Department of Management and Engineering, University of Padova, Stradella San Nicola 3, Vicenza 36100, Italy
[b] National Institute for Nuclear Physics (INFN) – Padua Division, via Marzolo 8, Padova 35131, Italy
[c] Brunel University London, Uxbridge, UK

ARTICLE INFO

Keywords:
Additive manufacturing
Cooling channels
Friction factor
Pressure drop
Surface roughness
Turbulent flow

ABSTRACT

The additive manufacturing capabilities open new frontiers in the design of complex geometries in many different application fields, especially thermal science, in which multi-functional, efficient, compact components with internal cooling or heating channels are becoming more and more requested. Among the possible additive manufacturing technologies, the laser powder bed fusion process has recently been proven to manufacture high-conductivity metals, with good mechanical and thermal properties (i.e. pure copper and copper alloys), attracting the attention of the heat transfer community. However, depending on the material, design, and process parameters, the surface roughness of the components can remarkably change and become a critical issue in cooling applications. Currently, the surface texture characteristics and the final channel size cannot be accurately estimated *a priori*, and thus the initial hypothesis of the current design methods may lead to unpredictable and undesired results. This work experimentally and numerically explores the effects of the building orientation on the fluid dynamic behaviour in CuCrZr alloy channels, which is considered one of the most promising additive manufacturing materials for thermal applications. By coupling the experimental hydraulic results with surface characterization and X-ray computer tomography dimensional measurements of the channels, a novel simplified methodology to properly correlate the pressure drop to the surface texture of a single wall is proposed and numerically validated.

1. Introduction

Additive manufacturing (AM) technology usually finds applications in small production, fast prototyping, and developing complex geometries that could not be manufactured using conventional techniques. A lot of different processes can be found in industry and in the open literature about metal additive manufacturing (MAM): material extrusion, binder jetting, powder bed fusion, and direct energy deposition [1]. Among the others, laser-based powder bed fusion of metals (PBF-LB/M), also simply known as laser powder bed fusion (L-PBF), can manufacture several metals, typically achieving good material properties after proper process parameters calibration. The number and size of the printed components via MAM are increasing, because bigger and faster L-PBF machines are being made available in the market [2].

This manufacturing process is based on a high-power laser source. It starts from metal powders that are distributed by means of a recoater, which refills the fabrication plane. The laser is focused to melt the metal powder and it follows a specific path to cover different areas, layer after layer. The stratification continues until the 3D components are built [3]. L-PBF has the advantage of manufacturing not only prototypes but also final products.

For instance, in the aerospace industry, Blakey-Milner et al. [4] reported how MAM served to produce many components in rockets and aircraft projects, showing the potentiality of such technology. Kerstens et al. [5] designed rocket engines with an optimized layout of internal cooling channels to improve the performance of the nozzle controlling the maximum temperature in the printed material and validating the performance of the nozzle part.

In the automotive industry, the L-PBF is under investigation to build new geometries to reduce the weight of vehicles [6] and optimize the fuel consumption in engine parts. Di Blasio et al. [7] tested a piston prototype to reduce fuel consumption (up to 80 %) and NO_x quantities in an optimized bowl piston geometry.

In thermal science, the L-PBF process is attracting a lot of interest in several sectors: heat exchangers with new geometries that improve the

* Corresponding author at: Department of Management and Engineering, University of Padova, Stradella S. Nicola 3, Vicenza 36100, Italy.
E-mail address: giacomo.favero.1@phd.unipd.it (G. Favero).

https://doi.org/10.1016/j.ijft.2024.100790

Available online 5 August 2024

Nomenclature

A_{fluid}	cross-section area of the channel [m^2]
A_f	frontal area of a single roughness element [m^2]
A_s	windward wetted surface area of a single roughness element [m^2]
A_{wet}	wall wetted fluid [m^2]
B	log-law intercept for a smooth wall [-]
b_m	spanwise roughness length [m]
C	waigh and Kind intercept [-]
C_{sk}	Boyle and Stripf constant [-]
$C_{\varepsilon 1}$,$C_{\varepsilon 2}$,C_{μ}	coefficients in approximated turbulent transport equations [-]
d_h	hydraulic diameter [m]
$d_{h,mp}$	hydraulic diameter with planes method [m]
E	constant of Eq. (54) [-]
ES	effective slope of the surface roughness [-]
f_D	Darcy friction factor [-]
f_F	fanning friction factor [-]
$\widetilde{F}(s_k)$, $\widetilde{G}(ES)$, $F(s_k)$, $G(ES)$	auxiliary functions
K	turbulence kinetic energy [$m^2\ s^{-2}$]
k	roughness height [m]
k_s	equivalent sand-grain roughness [m]
K_P	turbulence kinetic energy at the wall-adjacent cell centroid [$m^2\ s^{-2}$]
k^+	roughness Reynolds number based on roughness height, $k^+ = ku_\tau/\nu$ [-]
k_s^+	equivalent sand-grain roughness Reynolds number, $k_s^+ = k_s u_\tau/\nu$ [-]
k_u	kurtosis of the roughness profile [-]
l	length of tested channel [m]
L	slenderness parameter [-]
P_{wet}	border wetted fluid [m^2]
Δp	pressure drop [Pa]
Rq	root mean square of roughness profile [μm]
Ra	arithmetic average of roughness profile [μm]
Re	Reynolds number based with length scale hydraulic diameter [-]
$Re_{\sqrt{A}}$	Reynolds number based with length scale the root square of cross-section flow [-]
Rz	maximum height of roughness profile [μm]
$S_{mean,mp}$	mean cross-section area with planes method [m^2]
S_{mean}	mean cross-section area [m^2]
Sa	arithmetic average of surface roughness profile [μm]
Sp	maximum peak height of surface roughness profile [μm]
Sv	maximum valley depth of surface roughness profile [μm]
Sz	maximum height of surface roughness profile [μm]
Sq	root mean square of surface roughness profile [μm]
Ssk	Skewness of surface roughness profile [-]
Sku	kurtosis of surface roughness profile [-]
Sp_{US}	maximum peak height of the upward surface roughness profile [μm]
Sp_{DS}	maximum peak height of the downward surface roughness profile [μm]
$Sp_{av,wall}$	average of the maximum peak height of channel walls surface roughness [μm]
$Sp_{av,thin}$	average of the maximum peak height of thin walls surface roughness [μm]
S	surface area without roughness [m^2]
S_f	total frontal area of the roughness [m^2]
S_s	total windward wetted surface area [m^2]
s_m	streamwise roughness length [m]
s_k	Skewness of roughness profile [-]
$\boldsymbol{U}$	fluid velocity vector [m s^{-1}]
u	average fluid velocity [m s^{-1}]
U^*	dimensionless fluid velocity in wall unit [-]
u_τ	friction fluid velocity [m s^{-1}]
U_P	average velocity of the fluid at the wall-adjacent cell centroid P [m s^{-1}]
U^+	dimensionless fluid velocity, $U^+ = u/u_\tau$[-]
ΔU^+	roughness function [-]
V_{fluid}	fluid volume [m^3]
y^*	dimensionless wall distance in wall unit [-]
y_P	distance from the wall-adjacent cell centroid to the wall [m]
y^+	dimensionless wall distance, $y^+ = yu_\tau/\nu$ [-]
y	wall distance [m]

Greek symbols

Δ	statistic parameter of the roughness peaks number [-]
ε	dissipation rate of turbulence kinetic energy [$m^2\ s^{-3}$]
θ	building angle with horizontal plane [°]
κ	von-Kàrman constant ($\kappa \approx 0.41$) [-]
λ	roughness solidity parameter [-]
λ_s	wavelength of cut-off filter [μm]
λ_k	simpson density parameter [-]
Λ	dirling roughness parameter [-]
Λ_k	Waigh and Kind roughness parameter [-]
Λ_s	Sigal and Danberg roughness parameter [-]
$\Lambda_{s,modified}$	van Rij et al. roughness parameter [-]
μ	average dynamic viscosity [Pa s]
μ_t	eddy viscosity [Pa s]
ν	average kinematic viscosity [$m^2\ s^{-1}$]
ρ	average fluid density [kg m^{-3}]
σ_K,σ_ε	coefficients in approximated turbulent transport equations [-]
τ_w	wall shear stress [Pa]

heat transfer coefficient [8], novel enhanced surface configurations, such as lattice structures and gyroid shapes [9], internal complex cooling channel layouts for extremely high heat fluxes [10], heat sinks with novel fins [11] and heat transfer for thermal storage applications [12].

In fusion energy facilities, for example, the L-PBF technology, and MAM in general, is going to be adopted for the manufacturing of critical components, in particular those that have to reject huge amounts of heat, especially generated during the particles collisions with the wall. Hancock et al. [13] demonstrated the possibility of adopting MAM technology to design a novel layout cooling system for components in the fusion energy field. Numerical analyses showed a better temperature distribution under 5 MW m^{-2} heat flux cases, having even reduced the thermal stresses. Seltzman et al. [14] designed and manufactured a lower hybrid current drive Radio Frequency launcher using GRCop-84 in L-PBF. They investigated the resolution of the additive technology, scanning specific artifacts with X-ray computed tomography (XCT) to measure the deviations from CAD dimensions.

In fusion energy applications, as well as in most thermal applications, the interesting materials are those that have high thermal conductivity (i.e. >300 W m^{-1} K^{-1}). Among the different printable materials, the CuCrZr is a special copper alloy, which after post-process heat treatments can present high thermal conductivity and discrete mechanical properties. Several pieces of research have recently been published in the literature, showing how to manufacture CuCrZr via L-PBF.

Tang et al. [15] proposed a state-of-the-art review of CuCrZr and CuCrNb copper alloy that could be additively manufactured. Yang et al.

[16] measured thermal conductivity at room temperature of CuCrZr samples produced by L-PBF. The as-built samples showed a 101 W m^{-1} K^{-1} thermal conductivity, while 313 W m^{-1} K^{-1} was reached after a direct age-hardening heat treatment at 580°C in the oven.

Although unconventional and novel design cooling layouts can be manufactured, the MAM technology process is still limited in the geometrical tolerances and by the high surface roughness of the built channels as compared to conventional technologies (i.e. milling, turning) as described by Zanini et al. [17]. These two issues could negatively affect the heat transfer capabilities of novel cooling systems and they could also limit the design of these systems due to the unpredictable thermos fluid dynamic performance.

Ventola et al. [11] conducted a study on a heat sink for electronic cooling applications using air in a turbulent flow regime. The authors analysed different fins' performance varying the surface roughness. They experimentally measured the heat transfer coefficients and they compared the results with those obtained by conventional finned heat sinks. In general, if the coolant is in turbulent flow regime conditions, the friction factor and consequently the convective heat transfer coefficient are improved.

From the historical background, the hydraulic effects of the internal surface roughness were experimentally investigated by Nikuradse [18,19], which first investigated the friction factors in smooth pipes [18] and then correlated the friction factors in transitional and fully developed turbulent flows to the sand-grain roughness surface inside straight pipes [19]. The dimensions of the sand-grain roughness were carefully controlled because they were replicating a uniform roughness layer inside the studied pipes. Further, Colebrook and White [20] analysed the friction factor data obtained from commercial pipes, with a non-uniform sand-grain roughness size. They correlated the friction factors in fully developed turbulent flows with different relative roughness and Colebrook [21] proposed a correlation transition law as an appropriate empirical equation for the transitional and turbulent behaviour between smooth and roughned pipes. Nowadays, the Colebrook correlation [21] is the most applied equation for the estimation of the friction factors in commercial pipes and it was plotted by Moody [22,23] in the classic well-known diagram. It is reported the Colebrook correlation [21]:

$$\frac{1}{\sqrt{f_D}} = -2\log\left(\frac{k_s}{3.71 d_h} + \frac{2.51}{Re\sqrt{f_D}}\right) \tag{1}$$

where k_s is the absolute roughness index, or equivalent sand-grain roughness, and f_D is the Darcy friction factor.

During his studies, Nikuradse [18,19] identified three different flow regimes depending on the roughness effect: the "hydraulically smooth" regime whereas the fluid flow behaves like inside a smooth pipe, "transitionally rough" regime whereas the friction factor is a function of Reynolds number and relative roughness and "fully rough" regime whereas the friction factor is only a function of the relative roughness inside the pipe. Nikuradse also showed the logarithmic law of the wall in fluid flows:

$$U^+ = \frac{1}{\kappa} ln(y^+) + B - \Delta U^+ \tag{2}$$

Where y^+ is the dimensionless wall distance, defined as:

$$y^+ = y\frac{u_\tau}{\nu} \tag{3}$$

y is the distance from the wall, u_τ is the friction velocity, and ν is the average kinematic viscosity.

The friction velocity depends on the fluid density ρ and wall shear stress τ_w and it is defined as:

$$u_\tau = \sqrt{\frac{\tau_w}{\rho}} \tag{4}$$

There is a shift of the law that is present in rough pipes compared to the law valid for smooth ones. Nikuradse [19] defined a roughness function that modifies the logarithmic law of the smooth pipes for the rough ones in fully rough regime:

$$\Delta U^+ = B - 8.48 + \frac{1}{\kappa} ln(k_s^+) \tag{5}$$

Where κ is the von-Kàrman constant, B is the log-law intercept for a smooth wall, and k_s^+ is the equivalent sand-grain roughness Reynolds number, defined as:

$$k_s^+ = k_s\frac{u_\tau}{\nu} \tag{6}$$

Inspecting another pioneering work, Schlichting [24] defined the equivalent sand-grain roughness and validated it for predicting the friction factor of general roughened surfaces, starting from the Nikuradse data. He demonstrated that the inner velocity profile of a fully rough regime fluid collapses into Eq. (1) if the equivalent sand-grain roughness k_s is considered. To calculate it, the "reduction coefficient" $k_s\backslash k$ defined by Schlichting [24] is needed, where k depends on the roughness profile and is defined as maximum peak-to-valley height averaged over several subsets of the surface.

As investigated by Jimenez [25], Perry et al. [26], two different kinds of rough surfaces exist the k-type and d-type. For k-type roughness, Perry et al. [26] suggested that eddies with a length scale of order k (roughness height) are injected into the flow above the crest of the roughness elements which diffuse to the flow further away from the roughness crests, while d-type roughness maintains stable eddies between roughness elements. Jimenez [25] outlined two flow regimes: sparse and dense regime, depending on the roughness solidity parameter λ. In the sparse regime where the solidity is below λ = 0.15, the impact of the roughness increases with solidity, instead, in the dense regime the impact of roughness is reduced. These distinct behaviours are well explained in the review work by Kadivar et al. [27], the k-type with sparse regime (λ < 0.15) is most of the cases of surface roughness.

From Bettermann [28] the relationship of a spacing parameter λ, shape parameter of the roughness surface, defined as the pitch/height of 2D transverse bars for the estimation of the rough wall log-law intercept as reported:

$$f(\lambda) = B - \Delta U^+ + \frac{1}{\kappa} ln(k^+) = 17.35\ \left(1.165\log_{10}\lambda - 1\right) \qquad 1 \le \lambda \le 5 \tag{7}$$

Where k^+ is the roughness Reynolds number, based on maximum peak-to-valley height and defined as:

$$k^+ = k\frac{u_\tau}{\nu} \tag{8}$$

Dvorak [29] modified the relationship defining the density parameter λ as density parameter of the roughness surface and proposing these two relationships:

$$f(\lambda) = B17.35\ \left(1.165\log_{10}\lambda - 1\right) \qquad 1 \le \lambda \le 4.68 \tag{9}$$

$$f(\lambda) = -5.95\ \left(1.103\log_{10}\lambda - 1\right) \qquad \lambda > 4.68 \tag{10}$$

Moreover, although the Dvorak [29] and Bettermann [28] parameters were fitted on the experimental results of several surface roughness patterns [19,28,30], Simpson [31] proposed a new parameter λ_k as the total surface area/total roughness frontal area normal to the flow, confirming a fitting of the data of rough surfaces with staggered hemispheres [32], spheres and cones [33] and machined groves [34].

The combination of the two density and shape parameters was introduced by Dirling [35]. After having defined the combined density and shape parameter:

$$\Lambda = \left(\frac{d}{k}\right)\left(\frac{A_f}{A_s}\right)^{-4/3} \tag{11}$$

Where d and k are the average element spacing and the roughness height, respectively, for the density parameter, A_f is the frontal area of a single roughness element and A_s is the windward wetted surface area of a single roughness element. Dirling [35] proposed some correlations for the Schlichting reduction coefficient, to compute the sand-grain roughness height to the average roughness height:

$$\frac{k_s}{k} = 0.0164\ \Lambda^{3.78} \qquad \Lambda \le 4.93 \tag{12}$$

$$\frac{k_s}{k} = 139\ \Lambda^{-1.90} \qquad \Lambda > 4.93 \tag{13}$$

Sigal and Danberg [36] proposed a revised roughness parameter defined as:

$$\Lambda_s = \left(\frac{S}{S_f}\right)\left(\frac{A_f}{A_s}\right)^{-1.6} \tag{14}$$

Where S is the reference surface area before adding roughness and S_f is the total frontal area of the roughness.

For rough surface shapes bars, rods, and ribs, the correlations below were adopted:

$$\frac{k_s}{k} = 0.00321\ {\Lambda_s}^{4.925} \qquad 1.4 \le \Lambda_s \le 4.890 \tag{15}$$

$$\frac{k_s}{k} = 8 \qquad 4.890 \le \Lambda_s \le 13.25 \tag{16}$$

$$\frac{k_s}{k} = 151.711\ {\Lambda_s}^{-1.1379} \qquad 13.25 \le \Lambda_s \le 100 \tag{17}$$

Taking into reference the three-dimensional regular roughness, the modified correlations were proposed by van Rij et al. [37], including the data corrections from Coleman et al. [38]:

$$\frac{k_s}{k} = 1.583 \times 10^{-5}\ {\Lambda_s}^{5.683} \qquad \Lambda_s \le 7.842 \tag{18}$$

$$\frac{k_s}{k} = 1.802\ {\Lambda_s}^{0.03038} \qquad 7.842 \le \Lambda_s \le 28.12 \tag{19}$$

$$\frac{k_s}{k} = 255.5\ {\Lambda_s}^{-1.454} \qquad \Lambda_s > 28.12 \tag{20}$$

For three-dimensional irregular roughness, van Rij et al. [37] proposed a modified roughness parameter:

$$\Lambda_{s,modified} = \left(\frac{S}{S_f}\right)\left(\frac{S_f}{S_s}\right)^{-1.6} \tag{21}$$

where S and S_f are defined as Sigal and Danberg [36] before and $S_s$is the total windward wetted surface area, calculated numerically based on detailed surface profiles. To obtain the equivalent sand-grain roughness surface the correlations developed for regular three-dimensional roughness surface are adopted with the modified roughness parameter of Eq. (20) and Ra the average roughness height instead of the maximum peak-to-valley height k.

Additional correlations for three-dimensional roughness were proposed by Waigh and Kind [39], considering another formulation of the logarithmic law for walls from Eq. (2):

$$U^+ = \frac{1}{\kappa} ln\left(\frac{y}{k}\right) + B - \Delta U^+ + \frac{1}{\kappa} ln(k^+) = \frac{1}{\kappa} ln\left(\frac{y}{k}\right) + B - C \tag{22}$$

and the C intercept can be calculated by Waigh and Kind [39] correlations:

$$C = 10.56 \log_{10}\left[\lambda_k \left(\frac{k}{b_m}\right)^{0.87}\left(\frac{A_s}{A_f}\right)^{0.44}\right] - 7.59 \qquad \Lambda_k < 6 \tag{23}$$

$$C = -5.75 \log_{10}\left[\lambda_k \left(\frac{k}{b_m}\right)^{0.55}\left(\frac{A_s}{A_f}\right)^{1.38}\right] + 5.78 \qquad \Lambda_k > 6 \tag{24}$$

$$\Lambda_k = \lambda_k \frac{k}{s_m} \tag{25}$$

where λ_k is the density parameter of Simpson [31], $\frac{k}{s_m}$ is the streamwise aspect ratio, k is the roughness height and s_m is the streamwise roughness length, A_w is the roughness wetted area, A_f is the projected frontal area and b_m is the spanwise roughness length. Waigh and Kind [39] tuned their correlations on the results for a variety of roughness element shapes: cubes, blocks, flat plates, cylinders, rods, cones, spheres, and hemispheres.

In the applications of turbine blades, the possibility of defects on the surface like pitting, erosion and deposits going to modify the hydraulic performance of the turbine was investigated by Bons [40]. He used the Sigal and Danberg [36] parameter for irregular roughness to calculate the equivalent sand-grain roughness from the Schlichting reduction coefficient into the logarithmic term:

$$\log\left(\frac{k_s}{k}\right) = -1.31\ \log(\Lambda_s) + 2.15 \tag{26}$$

The methods reported before were collected in the literature reviews proposed by Flack and Shultz [41] and Kadivar et al. [27]. These methods are based on engineered surfaces with periodic surface patterns, and they utilised a wide range of roughness scales, including roughness height, pitch, density, and shape parameters, as described before. The relationship is given for the equivalent sand-grain roughness height as a function of the root-mean-square roughness height and the skewness of the roughness probability density function (PDF). Flack and Shultz [41] fitted the data in the literature for sandpaper [42], honed pipe [43], honed (scratch) [44], commercial pipe [45], gravel [46], different types of pyramids [47], packed spheres and packed spheres with grid [48] and they proposed this equation to evaluate the equivalent sand-grain roughness height:

$$k_s = 4.43\ Rq(1 + s_k)^{1.37} \tag{27}$$

Rq and s_k are the root mean square roughness height and the skewness of the roughness surface evaluation, respectively, from the PDF of the roughness profile.

In the case of negative skewness values, Flack et al. [49] modified the previous equation into:

$$k_s = 2.91\ Rq(2 + s_k)^{-0.284} \tag{28}$$

These proposals were derived from the statements of Bogard et al. [50] and Goodhand et al. [51]. Bogard et al. [50] showed that using a single roughness parameter, such as Ra, is insufficient for characterising roughness effects. The same Goodhand et al. [51] reported that previous criteria based only on the Ra values are underestimated for the hydraulic interactions with fluid flows. Thus, several research works defined the equivalent sand-grain roughness height from different parameters of the moment of surface height PDF [41,49,52,53], roughness slope [40,54], or density of the roughness elements [35,36]. In the investigations with random roughness, the work available in the open literature by Boyle and Stripf [52] correlates the characteristic of a probability density function of the roughness profile to compute the equivalent sand-grain roughness using the following:

$$k_s = 4.3\ Rq(1 + C_{sk} s_k) \tag{29}$$

C_{sk} is a constant slightly more than one, and for simplicity, this

constant is set to 1.0.

Simplified correlations to compute the equivalent sand-grain roughness in Colebrook and Nikuradse data is recently proposed by Botros [55]:

$$k_{s,\ Colebrook} = 1.306\ Rq + 0.078\ (Rq)^2 \tag{30}$$

$$k_{s,\ Nikuradse} = 2.294\ Rq \tag{31}$$

When considering the L-PBF process, many manufacturing process parameters can influence the resulting surface texture: the powder (e.g. material, composition, powder size distribution, and shape), the manufacturing process parameters (e.g. laser focus, laser power, scanning speed, scan strategy, hatching distances), the size and geometry of the printed parts, the position of the parts on the platform and the building orientation [56–59]. Klingaa et al. [60] analysed the surface textures of seven-channel samples, manufactured via L-PBF by varying the building angle from 0° to 90° for a total of seven-channel samples. They characterised the internal surface roughness of the channel by means of X-ray Computer Tomography (XCT), highlighting the presence of defects on the surface, such as spatters and semi-melted metal particles.

Using the L-PBF technology to manufacture components with embedded cooling channels, the analysis of the hydraulic and thermal behaviour caused by surface roughness is not easy predictable. With the small components that L-PBF can manufacture, the concept of embedded cooling channels with a reduction of the cross-section area was investigated by several researchers.

The surface roughness combined with small cross-section area channels can increase the interactions with fluid flows and heat transfer, specifically in mini-channels (channels with a hydraulic diameter d_h between 200 μm to 3 mm) and microchannels (channels with a d_h between 10 μm to 200 μm).

Kirsh and Thole [61] experimentally tested wavy cooling channels that have been numerically optimised for heat sink applications using air as a coolant. The L-PBF technology was used to manufacture the samples. They observed a high friction factor and Nusselt number for all the tested samples.

Concerning L-PBF mini-channels, Stimpson et al. [62] investigated the effect of surface roughness on the hydraulic and thermal performance of mini-channels for cooling of turbine blades made with Inconel 718. They compared the experimental results of friction factors and heat transfer coefficients of air flows in fully rough regimes with standard models for smooth ducts and they concluded that the Nusselt number is not linearly increasing as expected as the increasing of friction factor instead. Nevertheless, the using of L-PBF is a valid solution to implement the roughness into mini-channels and to obtain the same advantages in the cooling performance compared with channels with ribs and grooves. In the following work, Stimpson et al. [63] proposed the following correlation to predict the equivalent sand-grain roughness height valid for mini-channels manufactured via L-PBF:

$$\frac{k_s}{d_h} = 18\frac{Ra}{d_h} - 0.05 \qquad \frac{Ra}{d_h} > 0.028 \tag{32}$$

From the same research group, the works by Wildgoose et al. [64] provided experimental data of different channels sizes analysing the thermal and hydraulic performance of air cooling mini-channels in L-PBF Inconel 718. Wildgoose and Thole [65] tested nine different cross-section area shapes of mini-channel for turbine blades, printed at the 90° vertical building orientation. The hydraulic diameter and square root of the cross-sectional area were evaluated for both friction factor and Nusselt number. Differently from smooth channels, they found no differences in the scaling of friction factor or heat transfer results when using the hydraulic diameter or the square root of the cross-sectional area between the additively made channel shapes.

Wildgoose et al. [64] investigated experimentally the thermal and hydraulic performance of air flows in turbulent regime inside different sizes and building orientations mini-channels made via L-PBF. They observed significant variations in surface roughness and geometric deviations from the design CAD, for specific build directions and channel sizes. These differences influenced the friction factor and the Nusselt number, with an increasing of both with an effort correlation with the building angle, in particular, below 60°. When dealing with cooling ducts under 45° orientation, the thermal-hydraulic performance was strongly affected by the increased surface roughness and presence of defects.

When considering non-circular ducts, Duan et al. [66] proposed a new dimensionless parameter to estimate the pressure drop using a new characteristic length instead of the classical hydraulic diameter. Starting from the Blasius correlation [67] in smooth circular pipes:

$$f_F Re^{0.25} = 0.0791 \tag{33}$$

Where f_F is the Fanning friction factor, a quarter of the f_D Darcy friction factor as defined before.

Duan et al. [66] modified the definition of the Reynolds number, using the slenderness perimeter defined as geometric characteristic aspect ratio as follows:

$$L = \frac{P_{wet}}{4\sqrt{A_{fluid}}} \tag{34}$$

where P_{wet} is the total wetted perimeter and A_{fluid} is the flow area.

The modified correlation of Duan et al. [66] from Eq. (33) is reported below:

$$f_F Re_{\sqrt{A}}^{0.25} = 0.0767 \tag{35}$$

They showed that plotting the new correlation Eq. (35) versus $Re_{\sqrt{A}}$ fits the experimental data of smooth noncircular pipes better than using $fRe^{0.25}$ versus Re with an increasing of the predictability of 6 %.

Considering rough noncircular pipes, they proposed a modified version of the Colebrook correlation [21] as reported following:

$$f_F Re_{\sqrt{A}} = \left[3.6\log\left(0.2047\left(\frac{k_s}{\sqrt{A_{fluid}}}\right)^{10/9} + \frac{6.115}{Re_{\sqrt{A}}}\right)\right]^{-2} Re_{\sqrt{A}} \tag{36}$$

Other parameters can be found in literature to predict the equivalent sand-grain roughness for Colebrook correlation, with the application of CFD analyses. For example, Forooghi et al. [68] used direct numerical simulations to study the regular roughness surfaces effective slope $ES = 2\lambda$ parameter, defined by Napoli et al. [69], and inserted in the following correlations:

$$k_s = \begin{cases} R_z\ \widetilde{F}(s_k)\ \widetilde{G}(ES) & if\ \Delta \le 0.15 \\ R_z\ F(s_k)\ G(ES) & if\ \Delta > 0.15 \end{cases} \tag{37}$$

where:

$$F(s_k) = 0.67 s_k^2 + 0.93 s_k + 1.3 \tag{37a}$$

$$\widetilde{F}(s_k) = \begin{cases} F(s_k) & if\ \Delta \ge \Delta_0 \\ F(s_k)\ [1 + M(\Delta - \Delta_0)] & if\ \Delta < \Delta_0 \end{cases} \tag{37b}$$

$$G(ES) = 1.07\left[1 - e^{-3.5\ ES}\right] \tag{37c}$$

$$\widetilde{G}(ES) = 1.05\left[1 - e^{-3.8\ ES}\right] \tag{37d}$$

$\Delta_0 = 0.35$ and $M = 1.47 s_k^2 - 1.35 s_k - 0.66$ the constant values. The above correlations are valid for $0.2 < ES < 0.9$, $-0.33 < s_k < 0.66$, and $1.9 < k_u < 2.7$.

Taking into account cooling channels made via L-PBF with hydraulic diameter larger than 3 mm, Favero et al. [70] experimentally measured the friction factor of different shapes rough L-PBF cooling channels and

they proposed a procedure to calibrate the numerical fluid dynamic model of the rough channels to account for the equivalent sand-grain roughness of the L-PBF channels. In addition, Favero et al. [71] experimentally measured the friction factor of different shapes smoothed L-PBF cooling channels and they calibrated a CFD models to reproduce numerically the hydraulic behaviour.

In general, during the L-PBF process, once the powder (i.e. material, particle size distribution) and the process parameters are set, the surface texture can be mainly affected by the size of the part and by the building orientation [57–60,72–74].

The component orientation is a manufacturing variable that the operator can modify and control. The building orientation is commonly selected as the one that minimises the use of the support structures, which need to be removed with post-processes wasting time and material.

In complex cooling components with integrated cooling channels, the internal surfaces of the channels are not always aligned with the building orientation and, thus, the internal surface texture varies from wall to wall, affecting the final performance of the system. For example, all the non-vertical surfaces present the so-called upward-facing (up skin) surfaces or downward-facing (down skin) surfaces, which have a surface texture that remarkably depends on their orientation regarding the building one [59,60,62–64].

Since a standardized method to predict the surface texture in L-PBF upskin and downskin surfaces has not yet been proposed, it is a common strategy to investigate the effects of the building orientation by characterising different printed surfaces (i.e. thin walls) with different orientations [60].

In this work, the effects of the building orientation on the fluid dynamic behaviour of CuCrZr alloy channels, obtained using L-PBF technology, are investigated. Five channels with the same geometry built with building angles θ of 0° (horizontal), 45°, 60°, 75°, and 90°, as compared to the vertical building orientation are tested. Moreover, five thin walls with the same building angles were also manufactured close to their reference channels to investigate the possibility to characterise the surface texture using this simplified approach to develop a novel procedure to estimate *a priori* the fluid dynamic behaviour of 3D metallic channels using a conventional CFD numerical tool.

2. Materials and methods

2.1. Material and L-PBF process

The most common materials used in L-PBF processes, are weldable metal alloys that can be atomised in a stable powder state. The most studied and commercialised materials for L-PBF manufacturing technology are aluminum alloys, nickel and titanium alloys, stainless steels, cobalt alloys, and copper alloys [3,5,6,72,73]. In thermal science, the most important property is thermal conductivity, thus metals with high thermal conductivity are the most suitable. For example, particle-strengthened copper alloys such as CuCrZr and CuCrNb can achieve thermal conductivity values of 300–322 W m^{-1} K^{-1} [15] and 260–280 W m^{-1} K^{-1} [75], respectively. In addition, recent developments in laser technologies let to completely melt pure copper, achieving 99.3 % in relative density and 94.3 % International Annealed Copper Standard (IACS) for electrical conductivity, as reported by Jadhav et al. [76]. Other metals can be L-PBF processed when the cost is a limiting factor: aluminum alloys can be adopted in the thermal sector; Pracht et al. [77] experimentally tested and numerically simulated a 3D printed component for cryogenic applications. Fuchs et al. [78] additively manufactured heat exchangers for high-temperature applications using stainless steel 316L. They measured the friction factors and Nusselt numbers in laminar fluid flow regime.

In this study, a CuCrZr copper alloy is adopted because it can be easily printed, showing excellent thermal properties and high densities [15]. In addition, it has been proposed for fusion energy experiments [13]. The samples were manufactured via L-PBF using an EOSINT M280 machine by setting the printing parameters to achieve the maximum density. The feedstock material is a CuCrZr copper alloy with a 15–45 μm powder size distribution. The selected process parameters are laser power of 370 W, scan speed of 700 mm s^{-1}, hatching distance of 0.09 mm, and layer thickness of 20 μm. The scanning strategy involved stripes of 5 mm in width, and nitrogen was used as an inert gas in the building chamber during the manufacturing process. The density of the material was measured, using the ASTM Standard as the reference for the Archimedes principle [79]. Comparing the results with the CuCrZr alloy obtained via traditional technologies, the relative density of the material is 99.75 %.

2.2. Samples

As described before, five channels with the same geometry were built with building angles θ of 0° (horizontal), 45°, 60°, 75°, and 90°. For each oriented channel, a single 50×30 mm flat plate with a wall thickness of 1 mm was also manufactured. The channel is characterised by a square cross-section 4×4 mm. This shape was chosen to better investigate the influence of building orientation on both up-facing and down-facing surfaces. In Fig. 1a, the sizes of the channel prototypes are reported. The L-PBF versatility allowed us to include in the manufacturing process the pressure taps and connections to the hydraulic test apparatus. The distance between the pressure taps is 40 mm and their positions were defined by means of a sensitivity analysis carried out via CFD simulations, to reduce the possible inlet and outlet effects on the fluid flow. In Fig. 1b, the as-built samples are shown: the θ=90°, i.e. the vertical, and θ=75° oriented channels with their respective wall samples are visible. The samples were removed from the platform, the support machined off, and the hydraulic connections were then threaded. In Fig. 2a, the θ=45° oriented channel is also reported as an example.

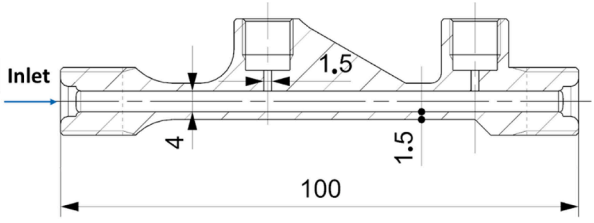

(a)

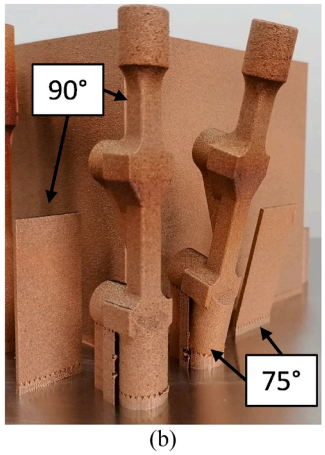

(b)

Fig. 1. Section view of the CAD model reports the main sizes (in mm) of the channel prototypes (a). The vertical θ=90° and θ=75° channel prototypes and the respective wall samples (b).

2.3. Experimental characterisation of the prototypes

The surfaces of the parts produced via L-PBF processes are typically characterised by complex texture and high surface roughness, with significant differences between up-facing and down-facing surfaces. In particular, the up-facing surfaces are commonly characterised by the combination of the staircase effect, the edge effect, and attached powder particles [80]. Differently, the down-facing surfaces are subjected to the combination of the same effects in addition to the building angle [81]. Support structures may mitigate these effects, but then they have to be removed increasing the complexity of the process and reducing the degree of freedom at the design stage.

The evaluation of the complex three-dimensional surface texture of AM parts can be carried out by means of optical profilometers [82]. In this work, a focus variation 3D optical profilometer Sensofar S neox (Sensofar Group, Spain) was used, with a 20× objective, to acquire three-dimensional surface topographies in 2×2 mm^2 regions on the thin wall samples and on the internal surfaces of the tested channels. In fact, after the experimental hydraulic tests, the channels were longitudinally cut into four parts (see Fig. 2b), by means of an electrical discharge machine, which ensures precise cuts and avoids possible contamination of the internal surfaces.

The acquired topographies were analysed in accordance with the international standard ISO 25178 [83] to compute the following areal surface texture parameters: *Sa, Sp, Sv, Sz, Sq, Ssk*, and *Sku*. In particular, the parameters were computed – as per the ISO standard – on the S-F surfaces, obtained by applying an F-operator based on the least-squares plane to remove the form error, and an S-filter with a cut-off λ_s equal to 2.5 μm to reduce the instrument noise.

(a)

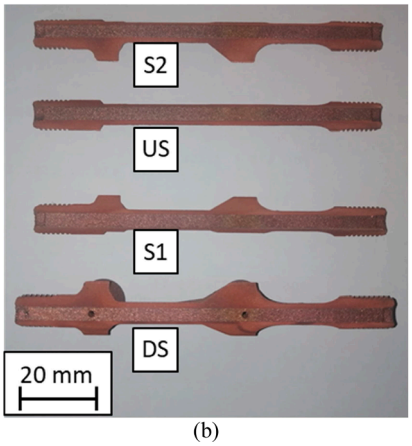

(b)

Fig. 2. Image of the θ=45° channel prototype before (a) and after the cuts (b). DS stands for DownSkin wall, while US stands for UpSkin wall, S1 and S2 are the two side walls.

Before the cut, the hydraulic section of each channel sample and hydraulic diameter were measured using the XCT technique. This was possible due to the small overall dimensions of the channel samples. In the literature there are different approaches aimed at reconstructing the shape and dimensions of the internal channels manufactured via MAM. Stimpson et al. [62] analysed the roughness effect on air flow and heat transfer of MAM channels. The channels were printed in a single orientation with respect to the building direction at 45°. They measured dimensions and roughness using XCT with high-resolution accuracy (±3.5 μm) and they reconstructed the internal shape of the channels fitting the XCT results by means of a polynomial function, reducing the peaks and valleys from the roughness profile. Another approach for measuring the hydraulic diameter and cross-section of the channel is proposed by Wildgoose et al. [64], and Wildgoose and Thole [65]. After the 3D construction of the XCT analysis, the cross-section and wet perimeter of the channels were computed averaging the result of 1200 slices taken along the streamwise axis of the channel. In the present work, an approach similar to Wildgoose et al. [64,65] was considered to measure the cross-sectional area and related perimeter, and the fluid flow volume and wetted surface, from the resolved XCT scans of each channel. The hydraulic diameter is the internal dimension of the channel that is related to the pressure drop of a cooling duct. The definition is given by:

$$d_h = \frac{4V_{fluid}}{A_{wet}} \tag{38}$$

where V_{fluid} is the fluid flow volume while A_{wet} is the wetted surface between solid and fluid. If the duct has a constant section the hydraulic diameter formula can be simplified into this:

$$d_h = \frac{4A_{fluid}}{P_{wet}} \tag{39}$$

where A_{fluid} is the cross-sectional area of the channel and P_{wet} is the perimeter of the cross-sectional area. In the present study, both definitions are used and reported.

The specimens were tested in a dedicated water loop test bench, collecting the pressure drop values by varying the water flow rate. The Reynolds number is defined as:

$$Re = \frac{\rho\ u\ d_h}{\mu} \tag{40}$$

where ρ is the average fluid density, μ the average dynamic viscosity of the fluid, and u is the average velocity of the fluid.

In turbulent fluid flow (i.e. Re>10000) for rough channels, the friction factor also depends upon the surface roughness of the pipe, as Moody's diagram [23] and Colebrook-White formula Eq. (1).

As the Reynolds number increases the second term in the brackets of Eq. (1) tends to zero and thus the friction factor becomes only a constant function of the absolute roughness index is relevant.

The pressure drop is related to the Darcy formula for fluid flows in pressure currents:

$$\Delta p = f_D \frac{l}{d_h} \frac{\rho u^2}{2} \tag{41}$$

in which l is the length of the considered pipe. This work investigates the effects of the surface roughness on frictional pressure drops. To correlate the building orientation of the manufacturing process with the different hydraulic behaviours, the surface roughness was measured on both the thin wall samples and the internal walls of each channel. One of the aims of this work is to demonstrate the possibility of using the surface roughness measured from thin wall samples, to have an accurate

roughness value of the internal walls of the printed channel.

3. Experimental results

3.1. XCT characterisation

The L-PBF process can result in significant deviations from theoretical CAD design as a function of the building orientation, especially in the case of internal complex channel. For this reason, XCT was used to measure the hydraulic diameter and the cross-sectional area of each sample. An XCT system Zeiss Metrotom 1500 (Carl Zeiss, Germany) was used to scan the entire channels, with an achieved voxel single-side dimension equal to 55 μm. The XCT reconstructions were analysed by extracting and then importing the STL file into the CAD software. Fig. 3 shows an example of a full XCT reconstruction. Seven transversal planes were considered to measure the cross-section of the channels and the mean value of these hydraulic diameters was then computed. In Fig. 3b, an example of the fluid volume portion is used to evaluate the hydraulic diameter with Eq. (39).

As shown in Fig. 3, two methods were used to evaluate the hydraulic diameter of the different 3D printed channels. The first, named multiple planes, evaluated the hydraulic diameter by averaging the measurements collected on seven transversal planes located along the channel, as shown in Fig. 3a. Thus, the mean cross-sectional area of each plan, $S_{mean,mp}$, is given by:

$$S_{mean,mp} = \frac{\sum_{n=1}^{7} A_{fluid}}{7} \tag{42}$$

where A_{fluid} is the cross-sectional area measured for a single transversal plane. The hydraulic diameter, $d_{h,mp}$, which is then:

$$d_{h,mp} = \frac{4\frac{\sum_{n=1}^{7} A_{fluid}}{7}}{\frac{\sum_{n=1}^{7} P_{wet}}{7}} \tag{43}$$

The second method refers to the entire fluid volume and the wetted area, evaluated from the XCT scans, to compute the hydraulic diameter d_h, as defined by Eq. (38). In this case the mean section area, S_{mean}, is simply calculated by dividing the hydraulic diameter by the length of the analysed channel l:

$$S_{mean} = \frac{d_h}{l} \tag{44}$$

The results of the two methods are reported in Table 1. As one can see, in most of the cases there are not any noticeable deviations between the two methodologies, meaning that both can be considered to evaluate the hydraulic diameter.

In fact, the deviation is always below ±2 % apart from that of the horizontally built channel, where the deviation is around ±5 %. This can be explained considering that the cross-sectional area of this sample is the most affected by the building orientation and the defects present on the internal surface of the channel can be of significant relevance for the channel. For these reasons, the authors decided to use the volume average method because it allows to better consider the morphology of the entire channel.

3.2. Hydraulic characterisation

In this paragraph, the experimental results collected during water flow inside the five channels are reported. The hydraulic tests of the samples were carried out in an experimental setup located at the Department of Management and Engineering of the University of Padua. The test bench is a water loop where the water temperature and flow rate can be independently controlled. The pressure drops were measured using a differential pressure transducer with an uncertainty (level of confidence two standard deviations) of ±0.065 % on the full scale of 1.5 bar. The water temperature was monitored through calibrated T-type thermocouples with an accuracy of ±0.05 K. The tests were run by varying the water flow rate from 0.7 to 11.5 l/min, and multiple data sets were collected by increasing and decreasing the water flow rate to verify the repeatability of the results. In Fig. 4 the pressure drop data is reported against the Reynolds number for the five tested channel samples.

As shown in Fig. 5, the hydraulic behaviour of the channels is typical of rough pipes, it is worth underlining that lowest pressure drops were

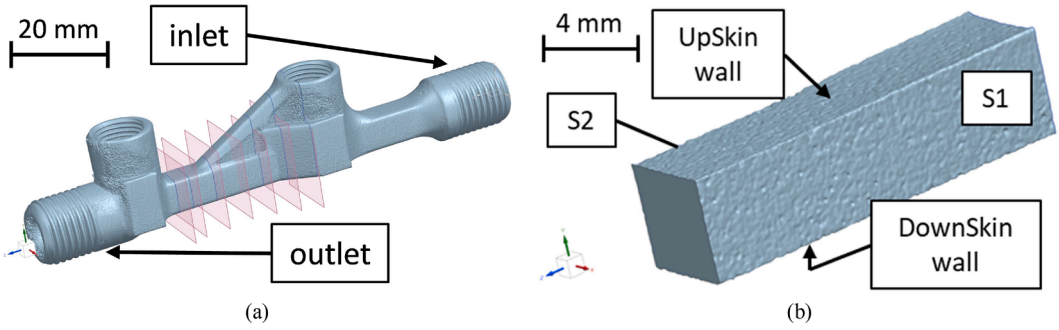

Fig. 3. XCT reconstruction of a vertically printed sample (θ=90°) with reference to the building platform. Comparison between the methods to evaluate the hydraulic diameter: multiple planes (a) and volume average (b).

Table 1
XCT dimensional measurements of the channels.

Method	Parameter	θ=90° (vertical)	θ=75°	θ=60°	θ=45°	θ=0° (horizontal)
Multiple planes	$S_{mean,mp}$[mm^2]	17.7	17.4	17.7	17.5	13.8
	$d_{h,mp}$ [mm]	4.15	4.10	4.19	4.12	3.28
Volume average	S_{mean} [mm^2]	17.6	17.4	17.7	17.2	13.7
	d_h [mm]	4.09	4.10	4.15	4.05	3.12

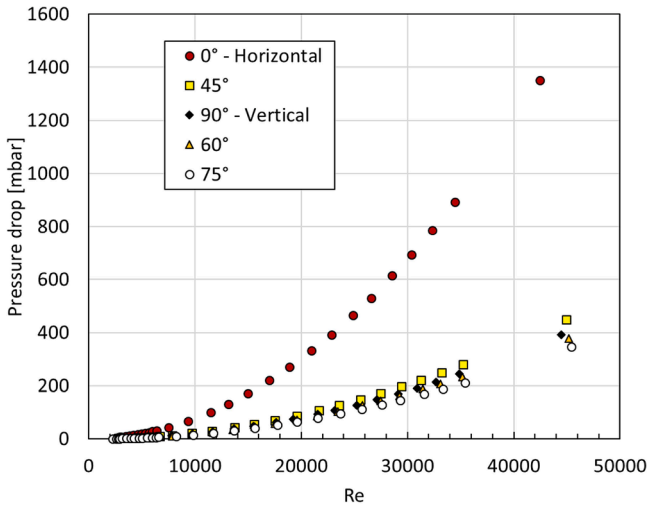

Fig. 4. Experimental frictional pressure drops plotted against Reynolds number.

exhibited by the θ=75° sample, while the horizontal one presented the highest values, which are extremely high from 3 to 4 times, as compared to the other samples. From Eq. (41), the Darcy friction factor can be computed using the experimental data. Δp is the experimental pressure drop, u is the water average velocity, computed from the mean section area S_{mean} and the measured water flow rate, $\rho = 996\ \mathrm{kg\ m^{-3}}$ is the mean water density, and d_h is the hydraulic diameter measured from the XCT scan (Table 1). The samples were tested in a Reynolds range that varies from 2400 to 44700, scouting transitional (i.e. $2300<Re<10000$) to turbulent flow regime (i.e. $Re>10000$). Fig. 5 presents the friction factor profiles, which are compatible with the expected behaviour for rough pipes as reported in the well-known Moody's diagram [23]. The zone of complete turbulence depends upon the absolute roughness index k_s of the inner surface of the channel. In the horizontal channel, the friction factor plateau starts at around Re=8000, while in θ=75°- 60°- 45°- 90°

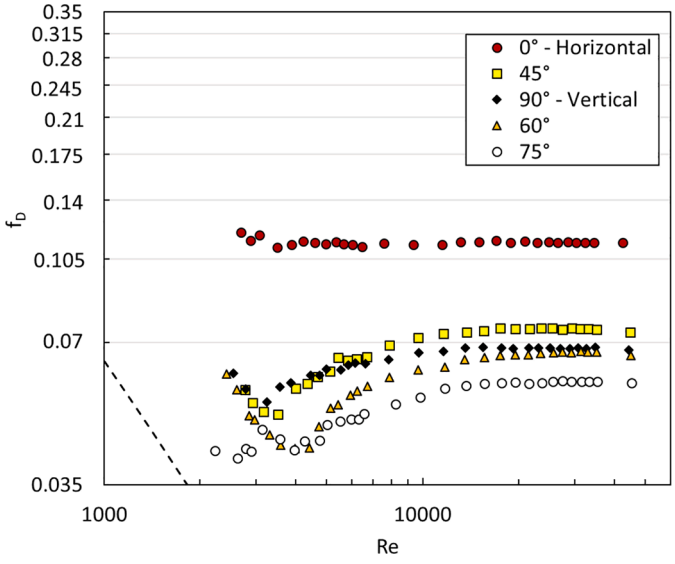

Fig. 5. Plot of the Darcy friction factor vs. Reynolds number. The calculated laminar flow friction factor (dotted line) is also plotted.

Table 2
Friction factors and absolute roughness indexes k_s of the tested samples.

	θ=90° (vertical)	θ=75°	θ=60°	θ=45°	θ=0° (horizontal)
f_D[-]	0.0680	0.0579	0.0667	0.0747	0.1140
k_s [mm]	0.179	0.122	0.173	0.218	0.380

channels, the plateau is reached when $Re>18000$.

In Table 2, the average friction factor values calculated in the zone of complete turbulence (Fig. 5) are reported. The channel sample with a θ=75° inclination exhibits the lowest friction factor, and the vertical specimen has a friction factor higher than θ=75° and θ=60°. Considering the definition of the absolute roughness index in the Colebrook-White formula Eq. (1), it is possible to compute a mean absolute roughness index k_s for each channel sample. In Table 2, the average absolute roughness indexes for the tested channels are also reported.

3.3. Surface analysis measurements

Fig. 6 reports the surface topographies of the four lateral walls of the channel samples, acquired as explained in Section 2.3. As a remark, US, S1, S2, and DS stand for Upskin, Side wall 1, Side wall 2, and Downskin, respectively. Fig. 6a shows that the four walls of the channels have similar topographies. In particular, the range bars specify that the peaks and valleys of the surfaces are distant less than 10 μm each other. It is possible to declare that in the vertical sample, the upskin and downskin effects are not present and, due to the high roughness of the surface texture parameters, from Fig. 6a, it is not easy to identify the building direction. Inspecting Fig. 6b, the horizontal channel has a completely different surface texture with respect to the vertical one. The upskin effect is strongly present and the side walls have almost the same topography as the side walls at θ=90°.

The areal surface texture parameters, computed from topographies are listed in Table 3.

From the analysis of the data reported in Table 3, it can be inferred that the best uniformity in terms of texture parameters is obtained at θ=75°. In general, all the other internal channels show different values of texture parameters, meaning that none of the internal surfaces can be considered representative of the surface texture of the channels obtained via L-PBF.

The surface texture parameters collected in Table 3 were used to calculate the equivalent sand-grain roughness height using different models available in literature. In Table 4, the results are showed and compared against the experimental data of equivalent sand-grain roughness heights. The values reported in Table 4 are the average sand-grain roughness height computed from the surface texture parameters of the four channels' walls. The values of *Sq*, root mean square height, were used for *Rq*, and *Sq*, arithmetic average surface roughness, for *Ra*. None of the models was able to fairly represent the experimental data. The deviations can be explained considering that the proposed models were regressed on different ranges of surface roughness which were remarkably different from that of the samples built in the present work. In particular, Botros [55] is valid for 2.7 μm<*Ra*<12.5 μm, Boyle and Stripf [52] equation calculates the equivalent sand-grain roughness based on roughness profile parameters tuned on regular 3D roughness and not random roughness profiles, while Flack and Shultz [41] equation is based on collected data available in the literature with 2.5 μm< *Rq*<1490 μm values. The results show deviations greater than 100 % for surfaces with *Rq*<5 μm [43], but the deviations reduce to 30 % for surfaces with similar L-PBF surfaces [44] *Rq*=26.4 μm (please note that

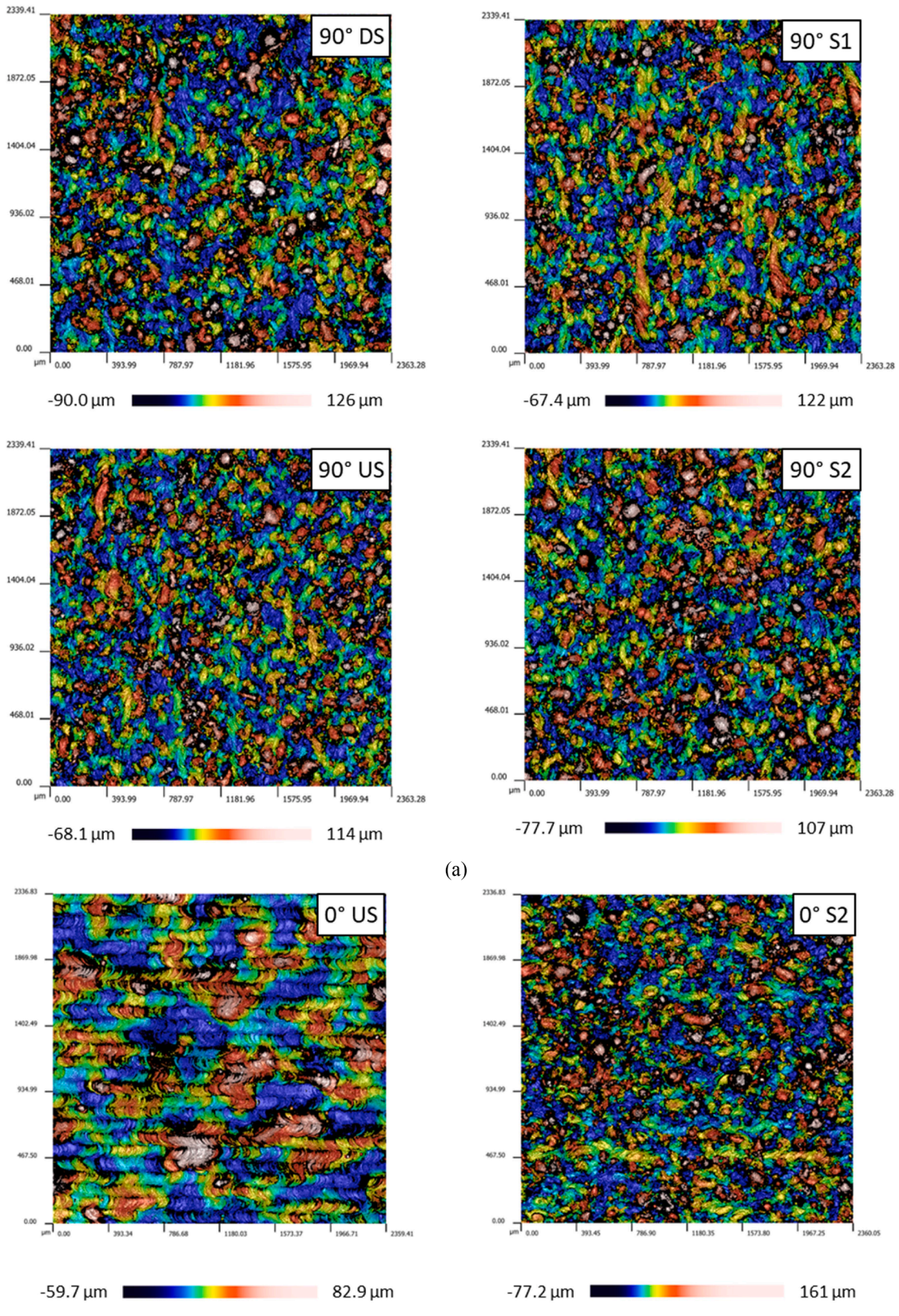

Fig. 6. Surface topographies of the channel specimens. In (a) the four lateral surfaces of the θ=90° channel sample are reported. In (b) the US and S2 walls of the horizontal channel.

Table 3
Areal surface texture parameters for the internal walls from channel samples.

	Surface orientation	*Sa* [μm]	*Sp* [μm]	*Sv* [μm]	*Sz* [μm]	*Sq* [μm]	*Ssk* [-]	*Sku* [-]
θ=90°	DS	23.4	126	90.0	216	29.6	0.74	3.65
	S1	18.9	122	64.7	184	24.6	0.90	4.24
	US	18.0	114	68.1	182	23.3	0.89	4.01
	S2	22.1	107	77.7	185	27.4	0.60	3.07
θ=75°	DS	19.9	104	84.1	188	25.1	0.60	3.41
	S1	19.1	113	73.3	186	26.0	0.96	4.33
	US	17.5	98.1	68.5	167	22.9	1.07	4.59
	S2	19.7	110	78.2	188	24.9	0.67	3.49
θ=60°	DS	19.2	138	67.9	206	24.33	0.62	3.71
	S1	19.4	155	72.8	228	25.8	1.24	6.00
	US	16.5	105	65.6	171	21.8	1.19	4.80
	S2	21.7	139	73.8	213	27.9	0.96	4.16
θ=45°	DS	25.4	153	87.0	240	32.8	0.78	4.14
	S1	24.8	167	90.7	258	33.1	1.31	6.34
	US	15.3	116	85.8	202	20.7	1.10	5.67
	S2	20.9	138	81.3	220	26.6	0.78	3.95
θ=0°	DS	127	383	385	768	127	-0.25	2.59
	S1	20.4	212	70.9	283	26.2	0.99	4.56
	US	15.2	82.9	59.7	143	19.3	0.26	3.33
	S2	18.3	161	77.2	238	23.8	0.93	4.65

Table 4
Equivalent sand-grain roughness height k_s, from different models in literature compared with the value measured from experimental friction factors.

		θ=90°	θ=75°	θ=60°	θ=45°	θ=0°
Experimental values	[mm]	0.179	0.122	0.173	0.218	0.380
Botros [55] Eq. (30)	[mm]	0.0884	0.0787	0.0815	0.102	0.415
Botros [55] Eq. (31)	[mm]	0.0602	0. 0561	0.0572	0.0650	0.113
Boyle and Stripf [52] Eq. (29)	[mm]	0.200	0.191	0.214	0.243	0.235
Flack and Shultz [41] Eq. (27)	[mm]	0.255	0.247	0.286	0.324	0.264
Stimpson et al. [63] Eq. (32)	[mm]	0.167	0.137	0.138	0.186	0.657

for negative skewness in θ=0° wall surface, Eq. (28) was adopted). Stimpson et al. [63] model, which was developed on measurements collected L-PBF channels with smaller diameter as compared to the current ones, shows interesting results with deviations ranging between 6 % and 75 %.

Moreover, there is another interesting result that can be highlighted: the data disprove the assumption that the side walls (S1 and S2) present almost the same roughness. In fact, only the θ=75° sample exhibits mean surface roughness values similar for the two side walls, all the others do not. Even if the surface quality depends mainly on its orientation with respect to the building direction, other factors can influence it. For example, the position on the platform could play an important role. Furthermore, the inert gas flow and the recoater directions could have an impact as well.

In order to study in detail the morphology and the causes of the high surface texture, the surfaces were also analysed with scanning electron microscopy (SEM). In Fig. 7, the images of four walls of the horizontal channel are reported. It is possible to recognise the main differences between the upskin and downskin surfaces. In particular, Fig. 7a shows the image taken at 100× for an unsupported down-facing surface region, where several surface cavities and solid powder particles are visible and those are the main ones responsible for the huge values of surface roughness reported in Table 3. Such complex morphology typically occurs in the first layers due to the so-called dross formation [84]: when the laser melts the first layer directly over the powder bed, the fused material does not find a solid handhold to attach above with adequate heat dissipation, and thus detached and irregular solid particles clusters are the result. The process might fail or continue with poor efficiency for several layers until a consistent solid material is built. In the experiments described in this work, the process was able to continue, but, as a general good practice, preventive actions should be taken, such as modifying the geometry, adding support structures, and tuning the laser parameters for specific downskin surfaces.

In Fig. 8, the images taken for the θ=45° channel walls are shown. It is possible to notice that, in the downskin surface (Fig. 8a), some not-completely melted particles are present on the surface. This is due to the overhang of the surface between one layer to another one, leading to the dross formation previously described. On the opposite side, the not-completely melted particles (Fig. 8c) are smaller, and thus the roughness values are lower as compared to the downskin region (see Table 3). The two side walls (Fig. 8b and d) are qualitatively quite similar in terms of dimensions of the defected not-completely melted particles attached to the surfaces; nevertheless, the surface texture parameters reported in Table 3 show that the *Sa, Sp, Sz, Sv* in S1 are slightly larger than in S2.

Fig. 9 illustrates the surface images taken for the θ=75° channel sample. The optical profilometer found similar results for all the internal four walls and in Fig. 9 there are no noticeable differences between the 4 images. In the case of the θ=75° channel sample, the combination of the building orientation, the recoater direction, and the set inert gas flow produced uniform and similar surface texture of all four internal walls,

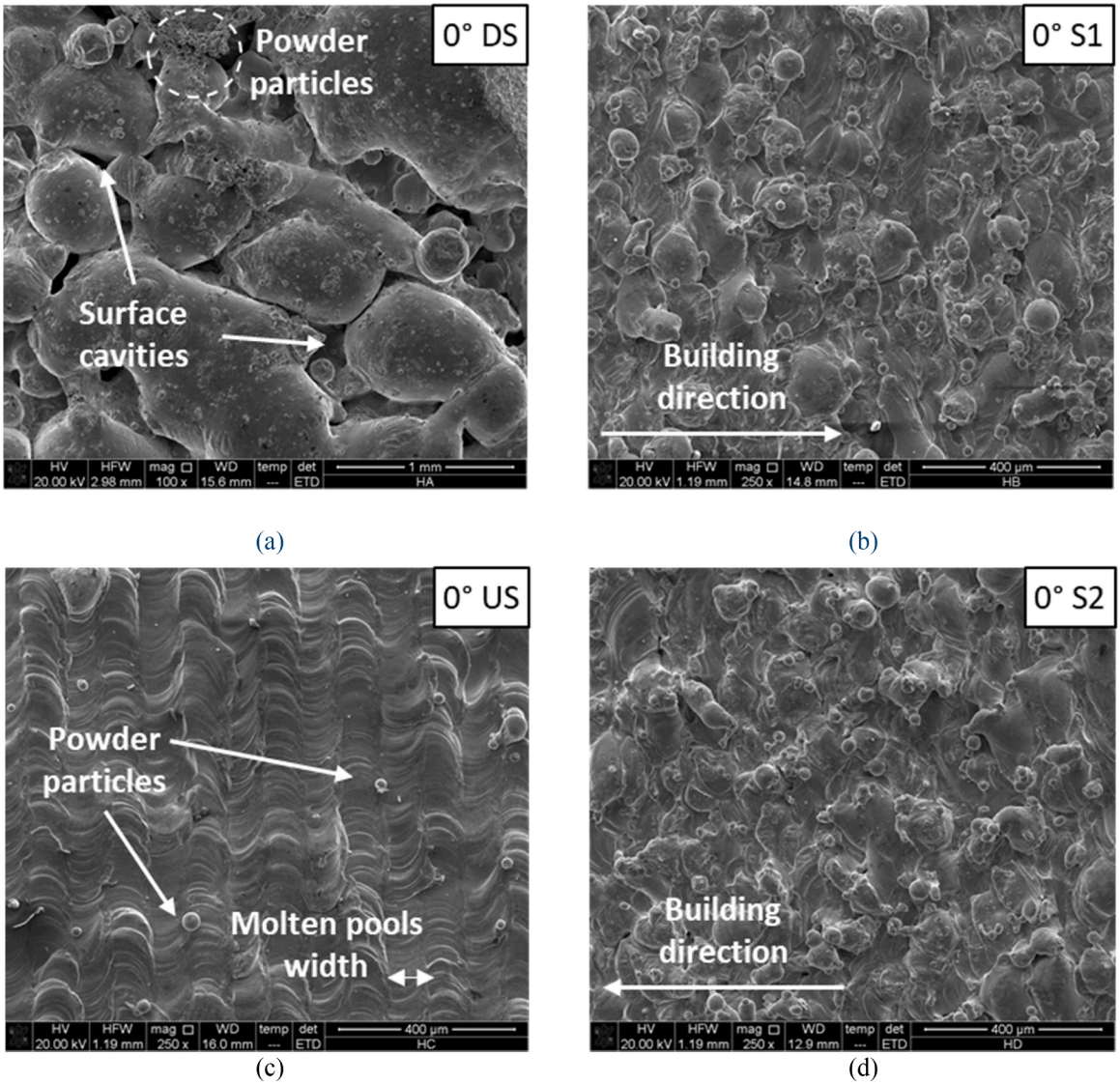

Fig. 7. SEM images of the four walls of the horizontal channel sample. In (a) 100× magnification of the downskin surface is reported. (b) and (d) show the side walls. In (c) the typical upskin horizontal surface with the molten pools directions can be recognised.

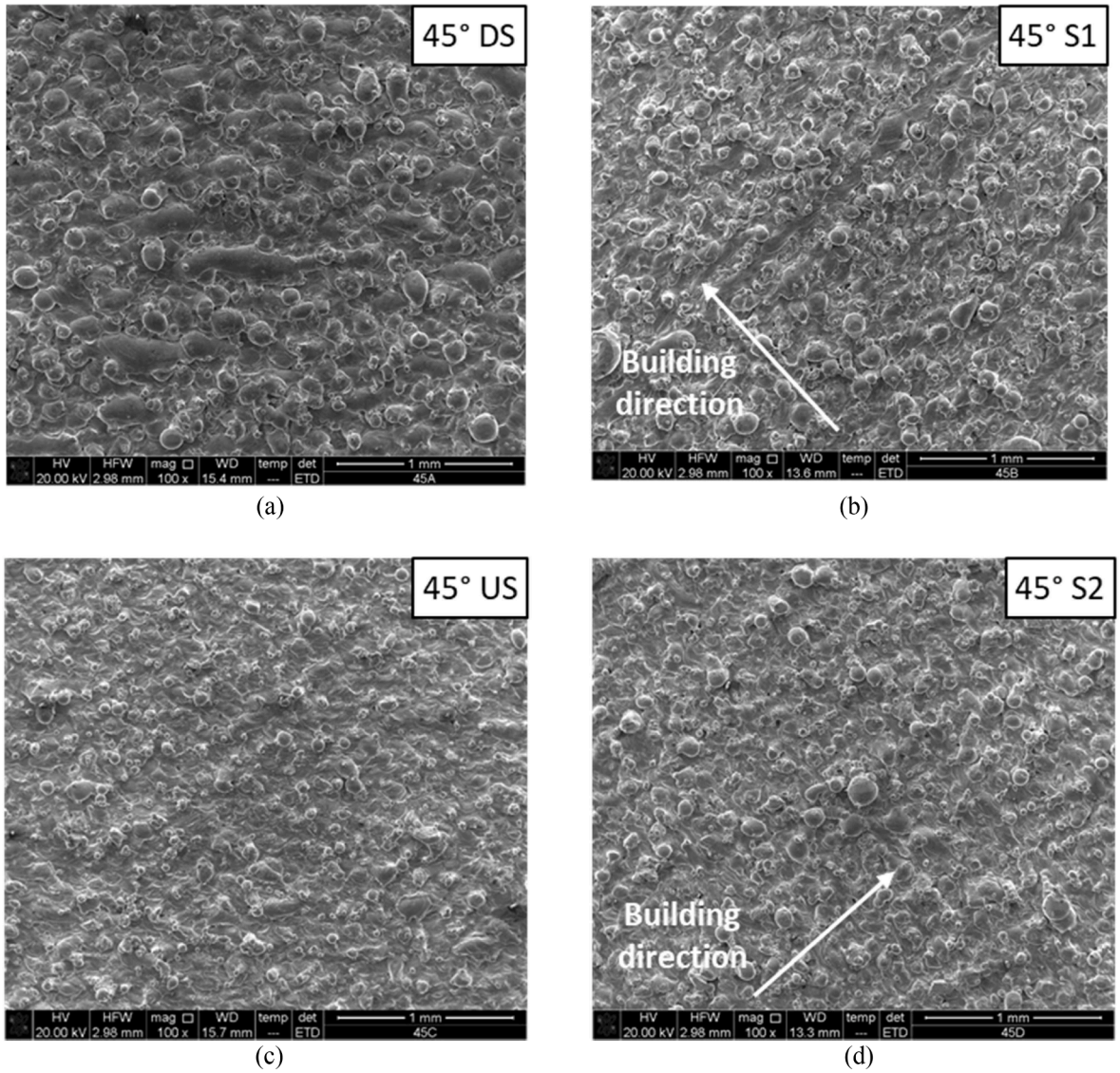

Fig. 8. SEM images of the four walls of the θ=45° channel sample. (a) refers to the downskin region; (b) and (d) to the side walls while (c) to the upskin surface.

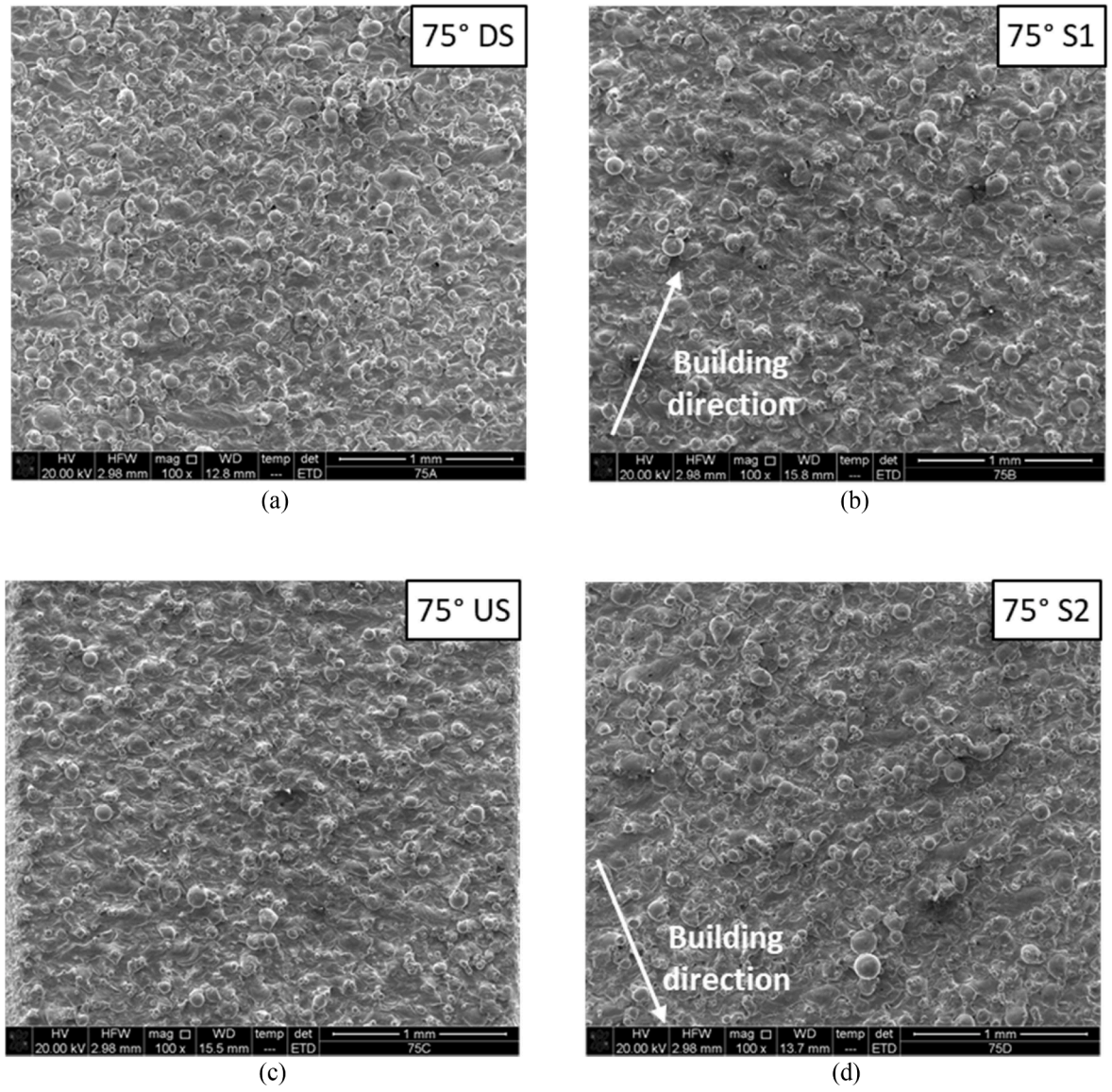

Fig. 9. SEM images of the four walls of the θ=75° channel sample. In (a), (b), (c), and (d) the downskin, side 1, upskin and side 2 walls are reported, respectively.

and this led to the lowest pressure drops and friction factors, as shown in Figs. 4 and 5, respectively.

The surface analysis was also conducted on the thin walls surfaces by means of the optical profilometer. As already mentioned, those walls were built with the same manufacturing process and building orientation. Fig. 10 shows the upskin and downskin surface topographies acquired for the horizontal and 45° walls, where several process defects (i.e. spatter particles and partially melted powder particles) attached to the surfaces can be observed. Similar defects can be recognised with respect to the same building orientation of the cut walls of the channels.

The collected database for the thin walls is summarised in Table 5.

Inspecting the data in Table 5, apart from the measurement collected for the θ=90° thin wall, the average values of the height parameter *Sa* (which is the areal texture parameter corresponding to the roughness parameter *Ra*, which instead is not measured over an area but on a 2D profile [83]) is higher on the DS surfaces than on the US surfaces. In the case of the θ=90° sample, it is the opposite, but this result is not confirmed by the analysis of the internal surfaces (see Table 3). To understand if the thin wall analysis can be considered a sufficiently accurate method to estimate the surface texture parameters of the 3D printed metal components, Table 5 also reports the percentage deviation between the data collected with the two independent methodologies.

In general, it can be stated that, in the case of US and DS surfaces, the texture parameters measured for the internal channels fairly agree with those collected for the thin walls, with deviations almost around or below ±10 %. In particular, the deviations for the *Sa* parameter are always below ±10 %. The largest deviations are found between the data sets for the horizontal thin wall and channel samples.

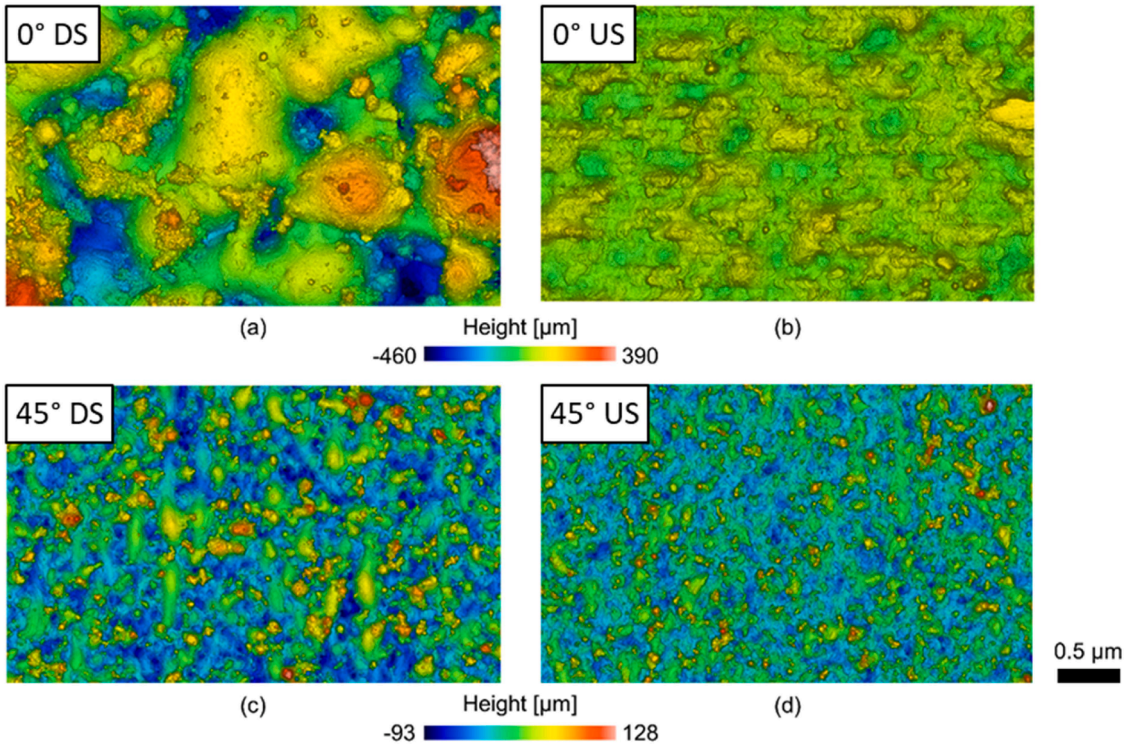

Fig. 10. Surface texture profiles for horizontal and θ=45° wall specimens. In (a) downskin and (b) upskin surfaces of horizontal thin wall, in (c) θ=45° downskin and (d) upskin surfaces.

Table 5
Areal surface texture parameters for thin wall samples.

	Surface orientation	*Sa* [μm]	Dev %	*Sp* [μm]	Dev %	*Sv* [μm]	Dev %	*Sz* [μm]	Dev %
θ=90°	US	22.9	-2.4	131	4.2	84.3	-6.3	216	-0.2
	DS	16.9	-6.0	130	14.0	71.8	5.6	202	10.8
θ=75°	US	19.1	9.6	125	27.4	71.5	4.4	197	17.9
	DS	19.7	-1.2	101	-2.9	85.3	1.4	186	-1.0
θ=60°	US	15.4	-6.4	122	15.5	64.9	-1.1	187	9.1
	DS	20.1	4.7	137	-0.5	86.2	27.0	224	8.5
θ=45°	US	14.9	-2.6	135	16.8	73.4	-14.5	209	3.5
	DS	23.5	-7.5	141	-7.8	92.9	6.8	234	-2.5
θ=0°	US	19.4	27.6	111	34.4	84.0	40.8	195	37.1
	DS	98.2	-22.6	391	2.1	458	19.0	849	10.5

3.4. Friction factor modelling

In general, the fluid flow inside rough pipes should be more influenced by the peaks of the surface texture rather than by the valleys, in which the fluid hardly flows. Thus, since the surface of the internal walls of the tested samples was fully characterised, it is possible to plot the experimental friction factors against the mean values of texture parameters. In fact, Fig. 11 plots the friction factors against the average values of *Sa, Sp, Sz*, and *Sv*, measured on the US and DS surfaces of the cut channel samples and of the thin walls.

It clearly appears that there is not any correlation between the mean surface roughness *Sa* and the friction factor. The surface texture parameters that seem to be significantly correlated to the friction factor are *Sz* and *Sp*. The *Sz* parameter quantifies the maximum peak-to-valley height, defined from the highest peak to the deepest valley, and hence is affected by the depth of the valleys *Sv*. A possible correlation $f_D = f(Sz)$ is shown in Fig. 11, but it seems not to well fit the experimental data for θ=75° and θ=45°. A better correlation $f_D = f(Sp)$ is here proposed to estimate the Darcy friction factor (for a fully turbulent fluid flow regime) as a function of the average *Sp* values using a logarithm function, as:

$$f_D = 0.0687 \ln Sp_{av,wall} - 0.2612 \qquad Re > 20000 \tag{45}$$

where the average value of the *Sp* measured on the upskin and downskin surfaces of the cut walls channel samples is computed as:

$$Sp_{av,wall} = \frac{Sp_{US} + Sp_{DS}}{2} \tag{46}$$

Eq. (45) is valid in a range of *Sp* which goes from 85 μm to 385 μm.

Moreover, it is also possible to correlate the Darcy friction factor (for a fully turbulent fluid flow regime) with the average *Sp*, measured on the thin walls, as:

$$f_D = 0.0702 \ln Sp_{av,thin} - 0.2735 \qquad Re > 20000 \tag{47}$$

Eq. (47) is valid in a range of *Sp* which goes from 100 μm to 390 μm.

As it can be seen, the proposed models fit very well the data with correlation coefficients equal to $R^2 = 0.9951$ and $R^2 = 0.9964$ for Eq. (45) and Eq. (47), respectively.

The deviations of the models as compared to the experimental values are summarized in Table 6. The models agree with the experimental data with a deviation always below ±4 %.

Both methods, starting from the surface roughness profile analysis,

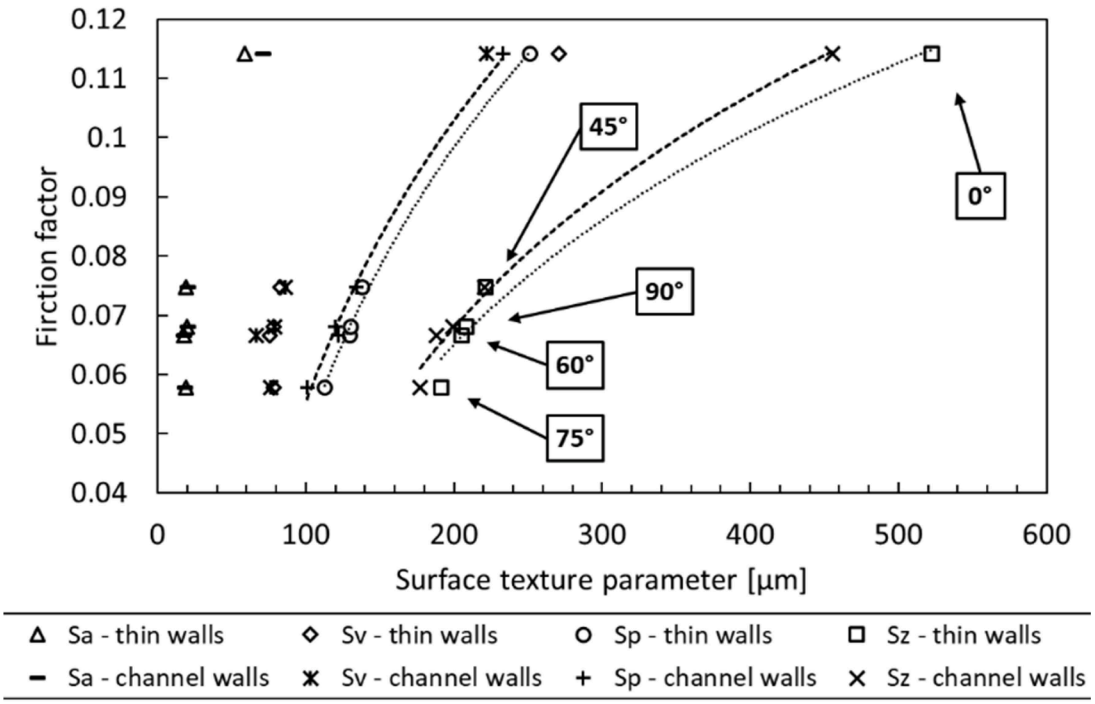

Fig. 11. Friction factor for fully rough turbulent flow (Table 2) vs. average value of US and DS surface texture results (Table 3 and Table 5). The dashed lines refer to the data for the cut walls, while the dotted lines refer to the data for thin walls.

Table 6
Deviations between the friction factors estimated with the proposed models in Eqs. (45) and (47), as compared to experimental data.

Orientation	f_D exp	f_D, Eq. (45)	Dev %	f_D, Eq. (47)	Dev %
θ=90°	0.0680	0.0677	-0.4 %	0.0685	0.7 %
θ=75°	0.0579	0.0559	-3.5 %	0.0584	0.8 %
θ=60°	0.0667	0.0686	2.8 %	0.0679	1.8 %
θ=45°	0.0747	0.0755	1.1 %	0.0724	-3.1 %
θ=0°	0.114	0.1133	-0.6 %	0.1144	0.3 %

gave similar maximum percentage deviations with the friction factors obtained from experimental results, thus the approach using one method to another one would estimate the friction factor with the same accuracy. The methodology is to support the method with the thin walls. The method that uses the thin walls' data to predict the friction factors seems to be a little bit more accurate and this confirms the suitability of this simple method to estimate the hydraulic behaviour of the 3D printed channels.

3.5. Numerical modelling

The experimental results of the friction factor obtained in the previous tests also allowed for calibrating a numerical model to accurately predict the pressure drops of the rough channels at different water flow rates, as already proposed by Favero et al. [70]. The commercial software Ansys Fluent was set to perform the three-dimensional fluid analyses in steady-state conditions. Ansys Fluent considers the Colebrook-White model to compute the friction factor in each volume element and to estimate the resulting pressure drop. Here, the equations used in the numerical model to solve the velocity field and pressure of the VOF model are reported.

Continuity equation:

$$\nabla\cdot\boldsymbol{U} = 0 \tag{48}$$

The Reynolds Averaged Navier-Stokes equations are solved based on the $K-\varepsilon$ turbulence model [85]:

$$\rho\boldsymbol{U}\cdot\nabla\boldsymbol{U} + \nabla\cdot(\overline{\rho\boldsymbol{u}'\otimes\boldsymbol{u}'}) = -\nabla P + \nabla\cdot\mu\left(\nabla\boldsymbol{U} + (\nabla\boldsymbol{U})^T\right) \tag{49}$$

The Partial Differential Equation (PDE) system is closed by the Eddy viscosity, defined:

$$\rho(\overline{\boldsymbol{u}'\otimes\boldsymbol{u}'}) = \frac{2}{3}\rho K - \mu_t\left(\nabla\boldsymbol{U} + (\nabla\boldsymbol{U})^T\right) \tag{50}$$

The transport equations for $K-\varepsilon$ are reported, respectively:

$$-\nabla\cdot\left[\left(\mu+\frac{\mu_t}{\sigma_K}\right)\nabla K\right] + \rho\boldsymbol{U}\cdot\nabla K = \frac{1}{2}\mu_t\left(\nabla\boldsymbol{U} + (\nabla\boldsymbol{U})^T\right)^2 - \rho\varepsilon \tag{51}$$

$$-\nabla\cdot\left[\left(\mu+\frac{\mu_t}{\sigma_\varepsilon}\right)\nabla\varepsilon\right] + \rho\boldsymbol{U}\cdot\nabla\varepsilon = \frac{1}{2}C_{\varepsilon1}\frac{\varepsilon}{K}\mu_t\left(\nabla\boldsymbol{U} + (\nabla\boldsymbol{U})^T\right)^2 - \rho C_{\varepsilon2}\frac{\varepsilon^2}{K} \tag{52}$$

The turbulent viscosity is defined:

$$\mu_t = \rho C_\mu\frac{K^2}{\varepsilon} \tag{53}$$

The PDE system is solved with the constants values which are reported from the wide turbulent flows condition that well fit the experimental data:

$$C_{\varepsilon1} = 1.44\ C_{\varepsilon2} = 1.92\ C_\mu = 0.09\ \sigma_K = 1.0\ \sigma_\varepsilon = 1.3$$

The geometry of each channel was tuned by comparing the CAD geometries with the XCT reconstructed ones (Table 1), which became the input geometry of the numerical simulation. Table 7 reports the

Table 7
Cross-sections and hydraulic diameters for each simulated geometry of channels.

	Square side [mm]	Hydraulic diameter [mm]	Cross-section [mm^2]	Cross-section dev %
θ=90°	4.046	4.092	16.368	-4.7
θ=75°	4.048	4.096	16.384	-3.6
θ=60°	4.073	4.146	16.584	-2.6
θ=45°	4.026	4.052	16.208	-4.7
θ=0°	3.562	3.124	12.496	-28.8

main geometrical characteristics used in the numerical model along with the deviations between the reconstructed XCT channels and the CAD geometries.

A mesh sensitivity analysis was carried out using Tetrahedrons element type into different element sizes. The analysis was developed at the maximum water flow rate, following the method proposed by Favero et al. [70]. Element sizes of 0.3 mm, 0.2 mm, and 0.15 mm were investigated in all the samples. For all the analyses refinement layers were included in the boundary layer of the turbulent water flow. A first layer thickness of 4 μm was set with a 1.2 growth rate, and a total of 17 layers were used. Besides, the inflation method was not necessary for the theory of boundary fluid flows [70]; in fact, here, the refinement was used keeping the same value of equivalent sand-grain roughness and changing the number of layers.

In Fig. 12 the three meshes with different element sizes are shown in a representative cross-section of the θ=75° channel.

The standard $K-\varepsilon$ turbulence model is applied with the Scalable Wall Function (SWF). The SWF is a standard wall function that is based on the work of Launder and Spalding [85].

The law of the wall is defined in Ansys Fluent based on the wall unit, y^*, rather than y^+:

$$U^* = \frac{1}{\kappa}\ln(Ey^*) \tag{54}$$

where the dimensionless velocity can be re-written:

$$U^* = \frac{U_P C_\mu^{1/4} K_P^{1/2}}{\tau_w/\rho} \tag{55}$$

The dimensionless distance from the wall is defined:

$$y^* = \frac{\rho C_\mu^{1/4} K_P^{1/2} y_P}{\mu} \tag{56}$$

Where κ is the von-Kàrman constant, E is an empirical constant equal to 9.793, U_P is the average velocity of the fluid at the wall-adjacent cell centroid P, K_P is the turbulence kinetic energy at the wall-adjacent cell centroid, y_P is the distance from the centroid of the wall-adjacent cell to the wall.

If $y^+ > 11.225$, the above SWF equations describe the law of the wall, instead, if $y^+ \leq 11.225$ the laminar relationship defines the fluid characteristics:

$$U^* = y^* \tag{57}$$

The law of the wall of the SWF is then modified considering roughness in the new intercept shift:

$$U^* = \frac{1}{\kappa}\ln(Ey^*) - \Delta B \tag{58}$$

Where ΔB is defined as a function of equivalent sand-grain roughness k_s in fully rough regime:

$$\Delta B = \frac{1}{\kappa}\ln(1 + C_s k_s) \tag{59}$$

The sand-grain roughness height value is the value obtained via the experimental results from Table 2. The adopted convergence criteria are set to 10^{-4} in the continuity and velocities residuals, while 10^{-6} in the k and epsilon residuals. In Table 8, the results of the mesh sensitivity analysis are shown for each sample. As one can infer, the mesh sensitivity analysis showed that even the coarsest grid is able to fairly predict the fluid flow behaviour of these rough channels except the horizontal channel. Thus, the 0.3 mm element size was adopted to decrease the computational efforts. It has to be pointed out that the numerical model of the 0° horizontal channel shows around 62 % deviations in pressure drops. This result can be explained by considering that the cross-section of the horizontal channel was deeply affected by the downskin wall, which partially collapsed. The real cross-section of this channel cannot be represented by a square cross-section.

The calibrated CFD models were then used to explore the entire tested Reynolds range (from 2300 to almost 50000). The numerical results in terms of pressure drops are plotted in Fig. 13. The curves of 90°-75°-60°-45° channels well fit the experimental data. The deviations of

Table 8
Mesh sensitivity analysis of the 5 samples. Deviations refer to the experimental data.

	Element size [mm]	N° elements	Roughness height [mm]	Pressure drop [Pa]	Dev %
θ=90°	0.3	826778	0.179	39017	-0.28
	0.2	2096125	0.179	38653	-0.42
	0.15	3387676	0.179	38736	-1.0
θ=75°	0.3	827345	0.122	34827	0.58
	0.2	2107831	0.122	34480	-0.42
	0.15	3372044	0.122	34545	-0.23
θ=60°	0.3	805072	0.153	36499	-3.6
	0.2	2129130	0.153	36183	-4.4
	0.15	3417004	0.153	36274	-4.2
θ=45°	0.3	815845	0.218	44096	-1.6
	0.2	2029122	0.218	43706	-2.5
	0.15	3348484	0.218	43817	-2.3
θ=0°	0.3	664553	0.380	218123	61.7
	0.2	1480703	0.380	218046	61.6
	0.15	2751764	0.380	219323	62.6

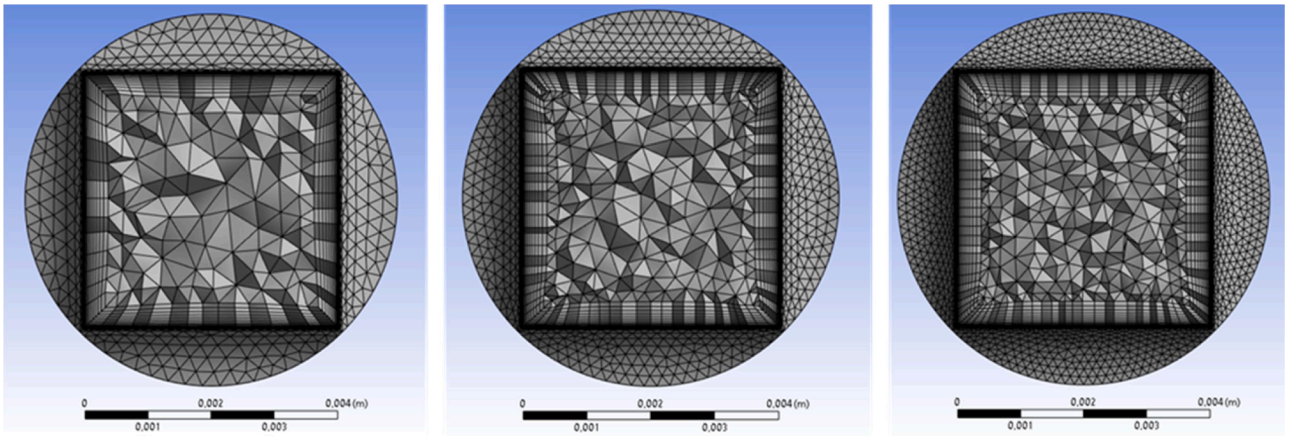

Fig. 12. Mesh cross-sections with different Tetrahedrons element sizes. In (a), (b), and (c) the 0.3 mm, 0.2 mm and 0.15 mm element sizes are reported.

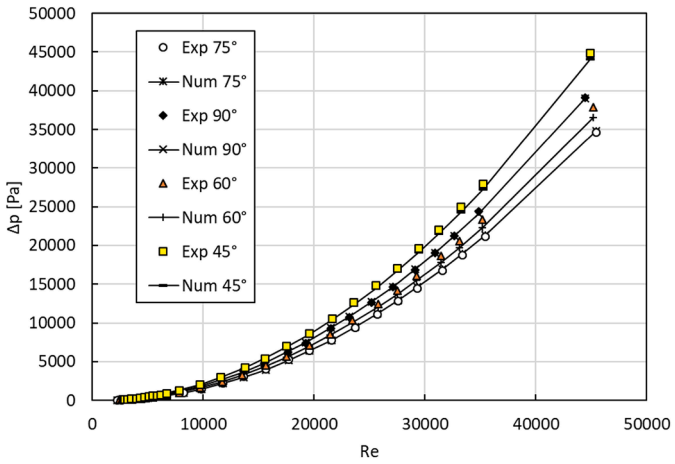

Fig. 13. CFD numerical results compared with the experimental data for specific channel, except horizontal channel.

the numerical models are lower than ±3 % for θ=90°-75°-45° when *Re*>10000, and ±5 % for θ=60°. In the range between of Reynolds number between 2300 and 10000, the θ=90° model gave numerical results with deviations lower than ±6 %, the θ=75° model lower than ±2 %, while the θ=60°-45° ones lower than ±10 %.

The plot reported in Fig. 13 shows that, using the RANS approach simulations, the equivalent sand-grain roughness value is needed to estimate properly the hydraulic behaviour of high internal roughness channels manufactured with the L-PBF process. The theory of the Colebrook equation is valid in fully turbulent regimes and for channels with hydraulic diameters bigger than 3 mm. Concerning the prediction using RANS approach, the size of the channel is important to be carefully taken into account such as the equivalent sand-grain roughness. The horizontal channel CFD results did not match the hydraulic values due to a not proper match of the geometry. As reported in Table 7, the square cross-section of the simulated channel is almost 30 % different from what XCT analysis reported. As a remark, the horizontal channel is here reported as a reference to the several issues that the construction of such a channel can bring. In fact, it is strongly affected by defects during the 3D printing process and, when possible, in the design phase of 3D printed components horizontal embedded cooling channels should be avoided, working with orientations range from 45° to 90°.

4. Conclusions

In this paper, a model to predict the friction factor in MAM channels for cooling applications is proposed. The work was meant to investigate, verify, and propose a methodology to predict *a priori* the pressure drops of L-PBF printed channels for further cooling applications.

Five channel samples were manufactured via L-PBF at different building orientations and experimentally characterised by measuring their hydraulic performance, their 3D geometry via XCT, and their surface texture via optical profilometer. Additional 5 thin walls were also printed with the same building orientation and the surface roughness was then characterised.

The friction factor results in a fully turbulent regime showed the minimum value at θ=75° of 0.0579, with an increase of 16-17 % for θ=60° and θ=90°, respectively, and an increase of 29 % for θ=45°. For the horizontal channel, the increase of the friction factor is more than twice compared with the lowest rough channel θ=75°.

The surface texture parameters from the surface analysis results were utilised to compute the equivalent sand-grain roughness height with the models available in the literature with the probability distribution function of the random surface roughness. The compared models did not match the range of applicability for the significant surface texture parameters of L-PBF surfaces obtained in this work. The equivalent sand-grain roughness was obtained from the literature models, and averaged between the four different surfaces, then compared with the experimental results of equivalent sand-grain roughness height using the Colebrook correlation Eq. (1). The results of the predicted equivalent sand-grain roughness showed significant differences because of outside the range of validity of the literature models, thus, a correlation was defined in terms of peaks of the surface roughness profile.

The results correlated the experimental friction factor to the surface texture of both the channels and the thin walls. The *Sp* surface texture parameter was found to be appropriate to be used to compute the friction factor in turbulent flow regime. The proposed models presented a maximum deviation of ±3 % for all the tested channels, which means *Re*>20000 and 100 μm<*Sp*<390 μm, and it confirms the possibility of predicting the pressure drop of conformal cooling channels with complex geometries built at different orientations (θ=0°-45°-60°-75°-90°). The match between the surface texture of the thin walls and the channels walls is possible if all the following are stated: same L-PBF process parameters, same metal powder, same building orientation, same wall thickness of the wall to the channel, and similar position to the building platform. Possible deviations can occur if the cross-section of the channels is different: circular, trapezoidal, triangular, etc. This could be investigated in further analyses, where the cross-sections of the channels may vary with respect to the single wall orientations.

Moreover, to avoid the need of printing multiple prototypes, the present work demonstrates that it is possible to print and characterise only thin walls surface as a function of desired building orientations. The surface roughness texture of these thin walls is representative of that of the much more complex channels, leading to accurate and reliable hydraulic design of the heat transfer devices.

Finally, the CFD analysis combined with the XCT analysis demonstrated that the equivalent sand-grain roughness from the Colebrook correlation of hydraulic tests is in accordance with the absolute roughness height of the CFD models, tuning the size channels with the XCT analysis. The equivalent sand-grain roughness height can be applied in further works to predict the hydraulic behaviour of tilted printed surfaces respect to the building orientation. In this work, surface characterisation has proved to be a reliable and accurate tool to predict pressure drops during turbulent water flows inside AM metal channels with high surface roughness.

CRediT authorship contribution statement

G. Favero: Writing – original draft, Validation, Methodology, Investigation, Data curation, Conceptualization. **M. Bonesso:** Writing – review & editing, Conceptualization. **R. Dima:** Supervision. **A. Pepato:** Supervision. **F. Zanini:** Writing – review & editing, Investigation, Data curation. **S. Carmignato:** Writing – review & editing, Supervision. **S. Mancin:** Writing – review & editing, Supervision, Methodology, Conceptualization.

Declaration of competing interest

The authors declare that they have no known competing financial interests or personal relationships that could have appeared to influence the work reported in this paper.

Data availability

The authors do not have permission to share data.

Acknowledgments

The authors would acknowledge the financial support of Fondazione Cassa di Risparmio di Padova e Rovigo (CariPaRo).

References

[1] M. Armstrong, H. Mehrabi, N. Naveed, An overview of modern metal additive manufacturing technology, J. Manuf. Proc. 84 (2022) 1001–1029, https://doi.org/10.1016/j.jmapro.2022.10.060.

[2] AMCM M4k, https://amcm.com/machines/amcm-m4k, 2024 (accessed 5 August 2024).

[3] D.D. Gu, W. Meiners, K. Wissenbach, R. Poprawe, Laser additive manufacturing of metallic components: materials, processes and mechanisms, Int. Mater. Rev. 57 (2012) 133–164, https://doi.org/10.1179/1743280411Y.0000000014.

[4] B. Blakey-Milner, P. Gradl, G. Snedden, M. Brooks, J. Pitot, E. Lopez, M. Leary, F. Berto, A. du Plessis, Metal additive manufacturing in aerospace: a review, Mater. Des. 209 (2021) 110008, https://doi.org/10.1016/j.matdes.2021.110008.

[5] F. Kerstens, A. Cervone, P. Gradl, End to end process evaluation for additively manufactured liquid rocket engine thrust chambers, Acta Astronaut. 182 (2021) 454–465, https://doi.org/10.1016/j.actaastro.2021.02.034.

[6] P. Nyamekye, S.R. Golroudbary, H. Piili, P. Luukka, A. Kraslawski, Impact of additive manufacturing on titanium supply chain: case of titanium alloys in automotive and aerospace industries, Adv. Ind. Manuf. Eng. 6 (2023) 100112, https://doi.org/10.1016/j.aime.2023.100112.

[7] G. Di Blasio, R. Ianniello, C. Beatrice, F.C. Pesce, A. Vassallo, G. Belgiorno, Additive manufacturing new piston design and injection strategies for highly efficient and ultra-low emissions combustion in view of 2030 targets, Fuel 346 (2023) 128270, https://doi.org/10.1016/j.fuel.2023.128270.

[8] I. Kaur, P. Singh, State-of-the-art in heat exchanger additive manufacturing, Int. J. Heat Mass Trans. 178 (2021) 121600, https://doi.org/10.1016/j.ijheatmasstransfer.2021.121600.

[9] L. Dassi, S. Chatterton, P. Parenti, A. Vania, B.M. Colosimo, P. Pennacchi, Cooled pads with bioinspired gyroid lattice for tilting pad journal bearings: Experimental validation of numerical model for heat transfer, Tribol. Int. 184 (2023) 108448, https://doi.org/10.1016/j.triboint.2023.108448.

[10] D. Kong, E. Jung, Y. Kim, V.V. Manepalli, K.J. Rah, H.S. Kim, Y. Hong, H.G. Choi, D. Agonafer, H. Lee, An additively manufactured manifold-microchannel heat sink for high-heat flux cooling, Int. J. Mech. Sci. 248 (2023) 108228, https://doi.org/10.1016/j.ijmecsci.2023.108228.

[11] L. Ventola, F. Robotti, M. Dialameh, F. Calignano, D. Manfredi, E. Chiavazzo, P. Asinari, Rough surfaces with enhanced heat transfer for electronics cooling by direct metal laser sintering, Int. J. Heat Mass Trans. 75 (2014) 58–74, https://doi.org/10.1016/j.ijheatmasstransfer.2014.03.037.

[12] A. Tamraparni, A. Hoe, M. Deckard, C. Zhang, N. Malone, A. Elwany, P. J. Shamberger, J.R. Felts, Design and optimization of composite phase change material for cylindrical thermal energy storage, Int. J. Heat Mass Trans. 208 (2023) 123995, https://doi.org/10.1016/j.ijheatmasstransfer.2023.123995.

[13] D. Hancock, D. Homfray, M. Porton, I. Todd, B. Wynne, Exploring complex high heat flux geometries for fusion applications enabled by additive manufacturing, Fusion Eng. Des. 136 (Part A) (2018) 454–460, https://doi.org/10.1016/j.fusengdes.2018.02.097.

[14] A.H. Seltzman, S.J. Wukitch, Resolution and geometric limitations in laser powder bed fusion additively manufactured GRCop-84 structures for a lower hybrid current drive launcher, Fusion Eng. Des. 173 (2021) 112847, https://doi.org/10.1016/j.fusengdes.2021.112847.

[15] X. Tang, X. Chen, F. Sun, P. Liu, H. Zhou, S. Fu, The current state of CuCrZr and CuCrNb alloys manufactured by additive manufacturing: a review, Mater. Des. 224 (2022) 111419, https://doi.org/10.1016/j.matdes.2022.111419.

[16] X. Yang, Y. Qi, W. Zhang, Y. Wang, H. Zhu, Laser powder bed fusion of C18150 copper alloy with excellent comprehensive properties, Mater. Sci. Eng. A 862 (2023) 144512, https://doi.org/10.1016/j.msea.2022.144512.

[17] F. Zanini, L. Pagani, E. Savio, S. Carmignato, Characterisation of additively manufactured metal surfaces by means of X-ray computed tomography and generalised surface texture parameters, CIRP Ann. 68 (1) (2019) 515–518, https://doi.org/10.1016/j.cirp.2019.04.074.

[18] J. Nikuradse, Gesetzmessigkeiten der turbulenten stromung in glatten rohren, Forschungsheft 356 (1932) volume B. VDI Verlag Berlin.

[19] J. Nikuradse, Stromungsgesetze in rauhen rohren, Forschungsheft 361 (1933) volume B,VDI Verlag BerlinTranslated in NACA Technical Memorandum nr. 1292, 1950.

[20] C.F. Colebrook, C.M. White, Experiments with fluid friction in roughened pipes, Proc. R. Soc. Lond. 161 (906) (1937) 367–381.

[21] C.F. Colebrook, Turbulent flow in pipes with a particular reference to the transition region between smooth and rough pipe laws, J. Inst. Civ. Eng. 11 (4) (1939) 133–156.

[22] Y.A. Çengel, J.M. Cimbala, Fluid Mechanics: Fundamentals and Applications, McGraw-Hill Education, Milan, 2015.

[23] L.F. Moody, Friction factors for pipe flow, Trans. ASME 66 (8) (1944) 671–678, https://doi.org/10.1115/1.4018140.

[24] H. Schlichting, Experimentelle untersuchungen zum rauigkeitsproblem, Ingenieur-Archiv 7 (1) (1936) 1–34.

[25] J. Jimenez, Turbulent flows over rough walls, Annu. Rev. Fluid Mech. 36 (2004) 173–196, https://doi.org/10.1146/annurev.fluid.36.050802.122103.

[26] A.E. Perry, W.H. Schofield, P.N. Joubert, Rough wall turbulent boundary layers, J. Fluid Mech. 37 (1969) 383–413, https://doi.org/10.1017/S0022112069000619.

[27] M. Kadivar, D. Tormey, G. McGranaghan, A review on turbulent flow over rough surfaces: fundamentals and theories, Int. J. Thermofluids 10 (2021) 100077, https://doi.org/10.1016/j.ijft.2021.100077.

[28] D. Bettermann, Contribtion a L'etude de la Couche Limite Turbulent le Long de Plaques Regueuses, Center National de la Recherche Scientifique, Report No. 65-6, 1965.

[29] F.A. Dvorak, Calculation of turbulent boundary layers on rough surfaces in pressure gradients, AIAa J. 7 (1969) 1752–1759.

[30] F.R. Hama, Boundary-layer characteristics for smooth and rough surfaces, Trans. SNAME 62 (1954) 333–351.

[31] R.L. Simpson, A generalized correlation of roughness density effects on the turbulent boundary layer, AIAa J. 11 (1973) 242–244, https://doi.org/10.2514/3.6736.

[32] D.K. Chen, and J.A. Roberson, The structure of turbulence in the wakes of roughness elements, ASCS Hydraulics Division 100(1), University of Iowa, Iowa City, IA, (1971), 10.1061/JYCEAJ.0003886.

[33] H. Schlichting, Boundary-Layer Theory, 7th ed., McGraw-Hill, New York, 1979.

[34] V.L. Streeter, Frictional resistance in artificially roughened pipes, Proc. ASCE 101 (1936) 681–713.

[35] R.B. Dirling, A method for computing rough wall heat transfer rates on Re-Entry Nosetips, AIAA Paper No. 73-763, (1973), 10.2514/6.1973-763.

[36] A. Sigal, J.E. Danberg, New correlation of roughness density effects on the turbulent boundary layer, AIAa J. 28 (1990) 554–556, https://doi.org/10.2514/3.10427.

[37] J.A. van Rij, B.J. Belnap, P.M. Ligrani, Analysis and experiments on three-dimensional, irregular surface roughness, ASME J. Fluids Eng. 124 (3) (2002) 671–677, https://doi.org/10.1115/1.1486222.

[38] H.W. Coleman, B.K. Hodges, R.P. Taylor, A re-evaluation of Schlichting's surface roughness experiment, ASME J. Fluids Eng. 106 (1984) 60–65, https://doi.org/10.1115/1.3242406.

[39] D.R. Waigh, R.J. Kind, Improved aerodynamic characterization of regular three-dimensional roughness, AIAa J. 36 (1998) 1117–1119, https://doi.org/10.2514/2.491.

[40] J.P. Bons, St and CF augmentation for real turbine roughness with elevated freestream turbulence, ASME J. Turbomach. 124 (4) (2002) 632–644, https://doi.org/10.1115/1.1505851.

[41] K.A. Flack, M.P. Schultz, Review of hydraulic roughness scales in the fully rough regime, ASME J. Fluids Eng. 132 (4) (2010) 041203, https://doi.org/10.1115/1.4001492.

[42] K.A. Flack, M.P. Schultz, J.S. Connelly, Examination of a critical roughness height for outer layer similarity, Phys. Fluids 19 (2007), https://doi.org/10.1063/1.2757708.

[43] M.A. Shockling, J.J. Allen, A.J. Smits, Roughness effects in turbulent pipe flow, J. Fluid Mech. 564 (2006) 267–285, https://doi.org/10.1017/S0022112006001467.

[44] M.P. Schultz, K.A. Flack, The rough-wall turbulent boundary layer from the hydraulically smooth to the fully rough regime, J. Fluid Mech. 580 (2007) 381–405, https://doi.org/10.1017/S0022112007005502.

[45] L.I. Langelandsvik, G.J. Kunkel, A.J. Smits, Flow in a commercial steel pipe, J. Fluid Mech. 595 (2008) 323–339, https://doi.org/10.1017/S0022112007009305.

[46] I.P. Castro, Rough-wall boundary layers: mean flow universality, J. Fluid Mech. 585 (2007) 469–485, https://doi.org/10.1017/S0022112007006921.

[47] M.P. Schultz, K.A. Flack, Turbulent boundary layers on a systematically varied rough wall, Phys. Fluids 21 (2009) 015104, https://doi.org/10.1063/1.3059630.

[48] M.P. Schultz, K.A. Flack, Outer layer similarity in fully rough turbulent boundary layers, Exp. Fluids 38 (2005) 328–340, https://doi.org/10.1007/s00348-004-0903-2.

[49] K.A. Flack, M.P. Schultz, J.M. Barros, Y.C. Kim, Skin-friction behavior in the transitionally- rough regime, Int. J. Heat Fluid Flow 61 (2016) 21–30, https://doi.org/10.1016/j.ijheatfluidflow.2016.05.008.

[50] D.G. Bogard, D.L. Schmidt, M. Tabbita, Characterization and laboratory simulation of turbine airfoil surface roughness and associated heat transfer, J. Turbomach. 120 (1998) 337–342, https://doi.org/10.1115/1.2841411.

[51] M.N. Goodhand, K. Walton, L. Blunt, H.W. Lung, R.J. Miller, R. Marsden, The limitations of using "Ra" to describe surface roughness, J. Turbomach. 138 (10) (2016) 101003, https://doi.org/10.1115/1.4032280.

[52] R.J. Boyle, M. Stripf, Simplified approach to predicting rough surface transition, J. Turbomach. 131 (4) (2009) 041020, https://doi.org/10.1115/1.3072521.

[53] A.J. Musker, Universal roughness functions for naturally-occurring surfaces, Trans. Can. Soc. Mech. Eng. 6 (1980) 1–6, https://doi.org/10.1139/tcsme-1980-0001.

[54] J. Bons, A critical assessment of Reynolds analogy for turbine flows, J. Heat Transf. 127 (2005) 472–485, https://doi.org/10.1115/1.1861919.

[55] K.K. Botros, Experimental investigation into the relationship between the roughness height in use with Nikuradse or colebrook roughness functions and the internal wall roughness profile for commercial steel pipes, J. Fluids Eng. Trans. ASME 138 (8) (2016), https://doi.org/10.1115/1.4032601.

[56] P. Fischmann, F. Schrauth, F. Zanger, Influence of particle size distribution on surface roughness in powder bed fusion - a contribution to increase resource efficiency, CIRP Ann. Manuf. Technol. (2023), https://doi.org/10.1016/j.cirp.2023.04.018.

[57] E. Cerri, E. Ghio, G. Bolelli, Effect of surface roughness and industrial heat treatments on the microstructure and mechanical properties of Ti6Al4V alloy manufactured by laser powder bed fusion in different built orientations, Mater. Sci. Eng. A 851 (2022) 143635, https://doi.org/10.1016/j.msea.2022.143635.

[58] S. Rott, A. Ladewig, K. Friedberger, J. Caspe, M. Full, J.H. Schleifenbaum, Surface roughness in laser powder bed fusion – interdependency of surface orientation and laser incidence, Addit. Manuf. 36 (2020) 101437, https://doi.org/10.1016/j.addma.2020.101437.

[59] J.C. Snyder, C.K. Stimpson, K.A. Thole, D. Mongillo, Build direction effects on additively manufactured channels, ASME J. Turbomach. 138 (5) (2016) 051006, https://doi.org/10.1115/GT2015-43935.
[60] C.G. Klingaa, T. Dahmen, S. Baier, S. Mohanty, J.H. Hattel, X-ray CT and image analysis methodology for local roughness characterization in cooling channels made by metal additive manufacturing, Addit. Manuf. 32 (2020) 101032, https://doi.org/10.1016/j.addma.2019.101032.
[61] K.L. Kirsch, K.A. Thole, Experimental investigation of numerically optimized wavy microchannels created through additive manufacturing, J. Turbomach. 140 (2) (2018) 021002, https://doi.org/10.1115/1.4038180.
[62] C.K. Stimpson, J.C. Snyder, K.A. Thole, D. Mongillo, Roughness effects on flow and heat transfer for additively manufactured channels, ASME J. Turbomach. 138 (5) (2016) 051008, https://doi.org/10.1115/1.4032167.
[63] C.K. Stimpson, J.C. Snyder, K.A. Thole, D. Mongillo, Scaling roughness effects on pressure loss and heat transfer of additively manufactured channels, J. Turbomach. 139 (2) (2017) 021003, https://doi.org/10.1115/1.4034555.
[64] A.J. Wildgoose, K.A. Thole, P. Sanders, L. Wang, Impact of additive manufacturing on internal cooling channels with varying diameters and build directions, ASME J. Turbomach. 143 (7) (2021) 071003, https://doi.org/10.1115/1.4050336.
[65] A.J. Wildgoose, K.A. Thole, Heat transfer and pressure loss of additively manufactured internal cooling channels with various shapes, ASME J. Turbomach. 145 (7) (2023) 071011, https://doi.org/10.1115/1.4056775.
[66] Z. Duan, M.M. Yovanovich, Y.S. Muzychka, Pressure drop for fully developed turbulent flow in circular and noncircular ducts, ASME J. Fluids Eng 134 (6) (2012) 061201, https://doi.org/10.1115/1.4006861.
[67] H. Blasius, Das Ahnlichkeitsgesetz bei Reibungsvorgangen in Flussigkeiten, VDI Forschungsheft 131 (1913) 1–12.
[68] P. Forooghi, A. Stroh, F. Magagnato, S. Jakirlic, B. Frohnapfel, Toward a universal roughness correlation, J. Fluids Eng. Trans. ASME 139 (12) (2017) 121201, https://doi.org/10.1115/1.4037280.
[69] E. Napoli, V. Armenio, M. De Marchis, The effect of the slope of irregularly distributed roughness elements on turbulent wall-bounded flows, J. Fluid Mech. 613 (2008) 385–394, https://doi.org/10.1017/S0022112008003571.
[70] G. Favero, M. Bonesso, P. Rebesan, R. Dima, A. Pepato, S. Mancin, Additive manufacturing for thermal management applications: from experimental results to numerical modeling, Int. J. Thermofluids 10 (2021) 100091, https://doi.org/10.1016/j.ijft.2021.100091.
[71] G. Favero, G. Berti, M. Bonesso, D. Morrone, S. Oriolo, P. Rebesan, R. Dima, P. Gregori, A. Pepato, A. Scanavini, S. Mancin, Experimental and numerical analyses of fluid flow inside additively manufactured and smoothed cooling channels, Int. Comm. Heat Mass Trans. 135 (2022) 106128, https://doi.org/10.1016/j.icheatmasstransfer.2022.106128.
[72] L. Deconinck, E. Bernardo Quejido, M.T. Villa Vidaller, E.A. Jagle, K. Verbeken, T. Depover, The mechanism behind the effect of building orientation and surface roughness on hydrogen embrittlement of laser powder bed fused Ti-6Al-4V, Addit. Manuf. 72 (2023) 103613, https://doi.org/10.1016/j.addma.2023.103613.
[73] F. Qiao, L. Wang, H. Li, Z. Li, B. Liu, P. Bai, Effect of structural parameters on the surface roughness and mechanical properties of Ti-6Al-4 V alloy thin-walled structure fabricated by selective laser melting, Mater. Today Commun. 39 (2024) 108977, https://doi.org/10.1016/j.mtcomm.2024.108977.
[74] K.L. Kirsch, K.A. Thole, Isolating the effects of surface roughness versus wall shape in numerically optimized, additively manufactured micro cooling channels, Exp. Therm. Fluid Sci. 98 (2018) 227–238, https://doi.org/10.1016/j.expthermflusci.2018.05.030.
[75] A.H. Seltzman, S.J. Wukitch, Nuclear response of additive manufactured GRCop-84 copper for use in Lower hybrid launchers in a fusion environment, Fusion Eng. Des. 159 (2020) 111726, https://doi.org/10.1016/j.fusengdes.2020.111726.
[76] S.D. Jadhav, L.R. Goossens, Y. Kinds, B. Van Hooreweder, K. Vanmeensel, Laser-based powder bed fusion additive manufacturing of pure copper, Addit. Manuf. 42 (2021) 101990, https://doi.org/10.1016/j.addma.2021.101990.
[77] S. Pracht, J. Will, S. Kloppel, T. Funke, H. Quack, C. Haberstroh, Experimental and numerical study of a 3D-printed aluminium cryogenic heat exchanger for compact Brayton refrigerators, Cryogenics 103418 (123) (2022), https://doi.org/10.1016/j.cryogenics.2021.103418 (Guildf).
[78] M. Fuchs, J. Bodemer, S. Kabelac, Experimental investigation of additively manufactured high-temperature heat exchangers, Int. J. Heat Mass Trans. 218 (2024) 124774, https://doi.org/10.1016/j.ijheatmasstransfer.2023.124774.
[79] Standard ASTM- B311-17, Standard Test Method for Density of Powder Metallurgy (PM) Materials Containing Less Than Two Percent Porosity. 2024.
[80] T.D. Ngo, A. Kashani, G. Imbalzano, K.T.Q. Nguyen, D. Hui, Additive manufacturing (3D printing): a review of materials, methods, applications and challenges, Compos. Part B 143 (2018) 172–196, https://doi.org/10.1016/j.compositesb.2018.02.012.
[81] A. Mirabal, I. Loza-Hernandez, C. Clark, D.E. Hooks, M. McBride, J.A. Stull, Roughness measurements across topographically varied additively manufactured metal surfaces, Addit. Manuf. 69 (2023) 103540, https://doi.org/10.1016/j.addma.2023.103540.
[82] W. Tato, L. Blunt, I. Llavori, A. Aginagalde, A. Townsend, A. Zabala, Surface integrity of additive manufacturing parts: a comparison between optical topography measuring techniques, Procedia CIRP. 87 (2020) 403–408, https://doi.org/10.1016/j.procir.2020.02.082.
[83] ISO 25178-2: 2021, "Geometrical Product Specifications (GPS) — Surface Texture: Areal — Part 2: Terms, Definitions and Surface Texture Parameters," International Organization for Standardization, Geneve.
[84] M. Baier, M. Sinico, A. Witvrouw, W. Dewulf, S. Carmignato, Unravelling the dependency of dross formations in metal additively manufactured channels as a function of channel diameter and inclination angle, CIRP J. Manuf. Sci. Technol. 45 (2023) 69–81, https://doi.org/10.1016/j.cirpj.2023.06.008.
[85] B.E. Launder, D.B. Spalding, The numerical computation of turbulent flows, Comput. Methods Appl. Mech. Eng. 3 (2) (1974) 269–289, https://doi.org/10.1016/0045-7825(74)90029-2.